

## TOOLS AND RESOURCES

# Real-time observation of light-controlled transcription in living cells

Anne Rademacher, Fabian Erdel\*, Jorge Trojanowski, Sabrina Schumacher and Karsten Rippe\*

### ABSTRACT

Gene expression is tightly regulated in space and time. To dissect this process with high temporal resolution, we introduce an optogenetic tool termed blue light-induced chromatin recruitment (BLInCR) that combines rapid and reversible light-dependent recruitment of effector proteins with a real-time readout for transcription. We used BLInCR to control the activity of a cluster of reporter genes in the human osteosarcoma cell line U2OS by reversibly recruiting the viral transactivator VP16. RNA production was detectable ~2 min after VP16 recruitment and readily decreased when VP16 dissociated from the cluster in the absence of light. Quantitative assessment of the activation process revealed biphasic activation kinetics with a pronounced early phase in cells treated with the histone deacetylase inhibitor SAHA. Comparison with kinetic models of transcription activation suggests that the gene cluster undergoes a maturation process when activated. We anticipate that BLInCR will facilitate the study of transcription dynamics in living cells.

This article has an associated First Person interview with the first author of the paper.

**KEY WORDS:** Histone acetylation, Nuclear organization, Optogenetics, Transcription regulation

### INTRODUCTION

Tools that enable the accurate control, visualization and quantification of the transcription process have driven recent progress in the field and are key to dissecting its molecular underpinnings. Tracing RNA by live cell imaging has provided a wealth of information on gene regulation and RNA processing (Cho et al., 2016; Darzacq et al., 2009; Larson et al., 2013; Martin et al., 2013). A system used in several of these studies is an array of reporter genes integrated into the human U2OS cell line (Janicki et al., 2004). It has been applied to investigate transcription activation and the associated changes in the chromatin environment (Janicki et al., 2004; Rafalska-Metcalf et al., 2010), as well as elongation and pausing of RNA polymerase II (Darzacq et al., 2007). However, it is difficult to investigate the early steps of the activation process and to assess its reversibility with existing techniques, which rely on chemicals for transcription initiation and, therefore, depend on diffusion and uptake/release of the respective compounds. To control protein interactions with high temporal precision a number of optogenetic methods have been adapted for use in mammalian cells (Tischer and Weiner, 2014). These include the CIBN-PHR system derived from the *Arabidopsis thaliana* proteins CIB1 (also known as BHLH63) and CRY2. Rapid binding of CRY2

or its photolyase homology region (PHR) to CIB1 or a truncated version of it (CIBN) can be induced by illumination with blue light (Kennedy et al., 2010). Different variations of the CIB1-CRY2 system have been exploited to recruit the VP64 transactivation domain to gene promoters marked by transcription activator-like effectors (TALEs) or dCas9 fusion constructs (Koneremann et al., 2013; Polstein and Gersbach, 2015). These systems did not include live-cell readouts for transcriptional activity and were, therefore, not suited to study the kinetics of transcription activation with high time-resolution in single cells. Here, we introduce a tool termed blue light-induced chromatin recruitment (BLInCR), which combines rapid and reversible binding of effectors with a real-time transcription readout in living cells. We used BLInCR to dissect the transcription activation process at a gene cluster and to probe the persistence of its activated state.

### RESULTS

#### Implementation of a light-inducible chromatin recruitment system

The BLInCR system is based on the PHR and CIBN domains of the *Arabidopsis thaliana* proteins CRY2 and CIB1 (Kennedy et al., 2010) that interact with each other when illuminated with blue light (Fig. 1A). Accordingly, CIBN fusion proteins that localize to nuclear structures or genomic loci of interest ('localizers') reversibly bind PHR fusion proteins ('effectors') upon exposure to blue light. To test the versatility of the BLInCR system we triggered and visualized the targeting of fluorescently labeled effector proteins to different nuclear subcompartments in the human U2OS 2-6-3 cell line (Janicki et al., 2004). It carries a stably integrated array of ~200 reporter construct units with promoter-proximal repeats of the *tetO* bacterial operator sequence. BLInCR robustly induced accumulation of PHR-mCherry as a mock effector at the reporter array, telomeres, nucleoli, PML bodies or the nuclear lamina (Fig. 1B, Table S1).

We then tested whether BLInCR is compatible with the U2OS 2-6-3 reporter system that allows the visualization of RNA transcripts in living cells. Their detection is based on a fluorescently labeled MS2 coat protein (MCP) that binds MS2 stem-loop sequences contained within the RNA transcripts (MS2-RNA) that are produced at the reporter gene array (Fig. 2A). The protein products encoded by these transcripts contain a cyan fluorescent protein (CFP) domain and localize to peroxisomes. We transfected cells with CIBN-TetR and the PHR-YFP-VP16 fusion protein, which comprises PHR, yellow fluorescent protein (YFP) and the strong viral VP16 transcription activation domain. Subsequently, cells were illuminated with blue light overnight, thereby constantly recruiting the activator to the array. We observed MS2-RNA accumulation at the reporter gene array and peroxisomal CFP expression in almost all illuminated cells (RNA: 92%, CFP-tagged proteins: 81%,  $n=37$ ; see Fig. 2B for a representative cell). We confirmed RNA production at these gene arrays by using RNA fluorescence in situ hybridization (FISH) with a probe directed against the MS2 loop sequences of the transcript (Fig. S1A,B). Furthermore, RNA polymerase II (Fig. 2C) and its Ser5-phosphorylated form (Fig. S2) were present at the reporter gene arrays activated by PHR-YFP-VP16 but not at silent arrays within

German Cancer Research Center (DKFZ) and Bioquant, Division of Chromatin Networks, Im Neuenheimer Feld 280, 69120 Heidelberg, Germany.

\*Authors for correspondence (karsten.rippe@dkfz.de; f.erdel@dkfz.de)

 F.E., 0000-0003-2888-7777; K.R., 0000-0001-9951-9395

Received 28 April 2017; Accepted 5 November 2017

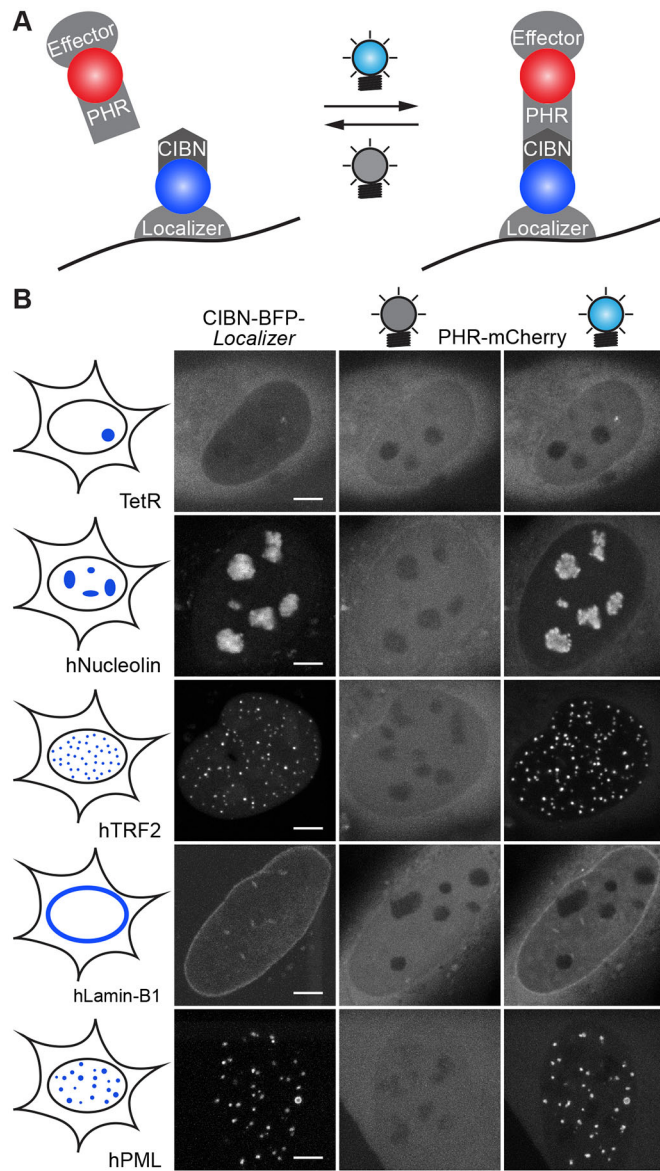


**Fig. 1. Blue light-induced chromatin recruitment (BLInCR).** (A) BLInCR is based on the interaction of the protein domains CIBN and PHR upon illumination with blue light. It allows binding of PHR-tagged effectors to CIBN-marked sites. The term ‘Localizer’ refers to a protein with a specific subnuclear localization with some examples shown in panel B. Red and blue circles represent fluorophores used for visualization. Only red and far-red fluorophores can be visualized without triggering recruitment. (B) BLInCR enables recruitment to different loci via the marker proteins given in brackets: *tetO* arrays (TetR), nucleoli (hNucleolin), telomeres (hTRF2), the nuclear lamina (hLamin-B1) or PML bodies (hPML splicing isoform III). PHR-mCherry (a mock effector) was homogeneously distributed throughout the cell before exposure (center column) and relocated to sites marked by CIBN-BFP-tagged localizers (left column) upon blue light exposure (right column). For each ‘Localizer’, 10 to 20 cells were imaged. Scale bars: 5  $\mu$ m.

cells that expressed a fusion protein comprising PHR, YFP and a nuclear localization sequence (PHR-YFP-NLS) as a control. To assess if activation affects other genes beyond the reporter, we performed RNA sequencing (RNA-seq) in non-transfected cells and in cells transfected either with CIBN-TetR and PHR-YFP-VP16 or with RFP-TetR and YFP (control). All cells were illuminated with blue light following transfection. Transfection with CIBN-TetR and PHR-YFP-VP16 induced robust activation of the reporter.

Virtually no additional changes of gene expression were observed beyond those seen in the control sample transfected with RFP-TetR and YFP (Fig. S3). Accordingly, we conclude that, in this respect, BLInCR behaves like other techniques that involve TetR.

**Kinetics of light-induced chromatin association and dissociation**

To characterize the kinetics of light-induced association and subsequent dissociation of the VP16 effector protein at the reporter array, we transfected cells with a CIBN-TetR construct and a fluorescently labeled PHR-VP16 fusion. To quantify the association reaction, we first identified the gene array by using RFP-tagged CIBN-TetR excited by green laser light that does not induce optogenetic recruitment. Subsequently, the binding of YFP-labeled PHR-VP16 was induced with blue laser light and monitored at 200 ms time resolution (Fig. S4A, Movie 1). Half-maximal levels were reached after  $13.6 \pm 4.9$  s (Fig. 2D), which is about one or two orders of magnitude faster than doxycycline- or tamoxifen-induced recruitment, respectively (Normanno et al., 2015; Rafalska-Metcalf et al., 2010). These estimates refer to moderate expression levels (~100 nM) of the recruited component. YFP-labeled PHR fused to either the NLS or the human histone acetyltransferase GCN5 (also known as KATA2A) accumulated with similar kinetics (Fig. S4B, Table S2). Induced accumulation of the respective fusion protein at the array occurred fast with two characteristic rates (Table S2). They might reflect the kinetics of the CIBN-PHR interaction and the previously described PHR oligomerization (Bugaj et al., 2013), which are both triggered by blue light. To quantify the dissociation reaction, PHR-mCherry-VP16 was targeted to the reporter array in cells expressing CIBN-TetR by illumination with blue light for 38 s (Fig. S4C). Subsequently, the loss of the mCherry signal from the array was monitored over time, showing a characteristic half-life of  $4.9 \pm 0.8$  min (Fig. 2E), which was identical for PHR-mCherry-NLS ( $4.8 \pm 0.6$  min, Fig. S4D, Table S3). Notably, the effectors were not detectable at the array 15–20 min after removing the light trigger.

**Quantification of transcription activation**

Next, we used BLInCR to follow the transcription activation kinetics of the array of reporter genes in U2OS 2-6-3 cells with high temporal resolution. RNA polymerase II was present at the array only a few seconds after activation (Movie 2). Low RNA levels were already detectable after about 2 min (Fig. 3A), followed by a lag phase with little or no additional RNA accumulation (Fig. 3B, gray line). After 20–30 min, a second phase of rapid accumulation of reporter RNA was observed, indicating that the activation process involves at least two distinct time scales. To assess the influence of activating chromatin marks on the activation kinetics we treated cells with the histone deacetylase inhibitor suberoylanilide hydroxamic acid (SAHA), which led to globally elevated levels of histone acetylation (Fig. 3C). Local enrichment of histone acetylation has previously been shown to coincide with transcriptional activation of the reporter array genes (Rafalska-Metcalf et al., 2010) and was also observed when activating transcription using BLInCR overnight (Fig. S5A-C). Cells that had been pre-treated with SAHA exhibited a much more pronounced fast activation phase (Fig. 3B, red line), suggesting that pre-existing histone acetylation facilitates the activation process. These results are consistent with the notion that some of the ~200 copies of reporter genes are poised for immediate activation, and that this fraction can be increased by hyperacetylation of histones in SAHA-treated cells. It has been reported that SAHA elicits a complex cellular response beyond histone hyperacetylation (Johnstone and Licht, 2003). In particular, it was shown that a number of non-histone

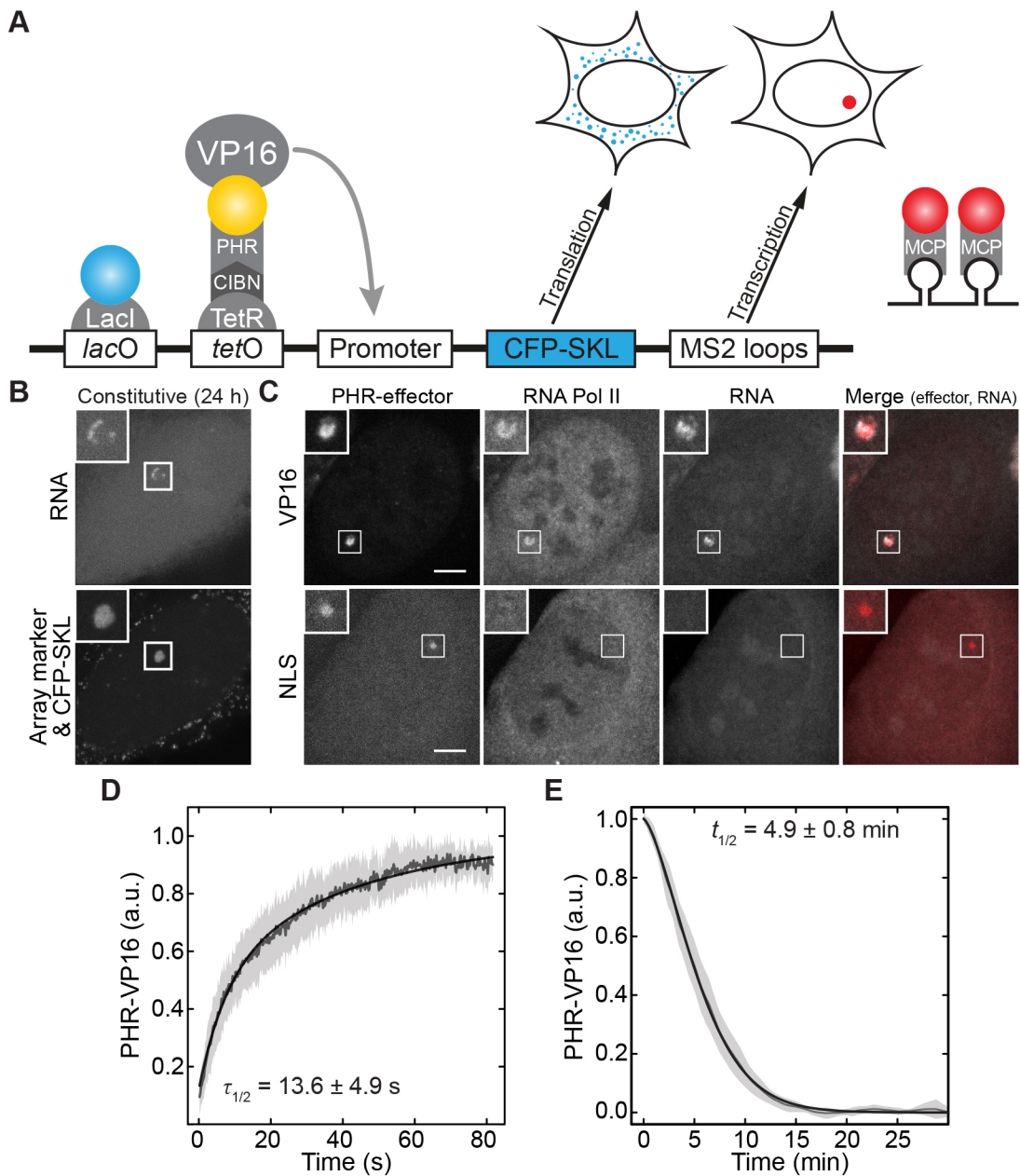


**Fig. 2. Dynamic transcription control by BLInCR.** (A) Schematic representation of the reporter system used to detect transcription in real time (Janicki et al., 2004). Transcription of the array of reporter genes can be monitored by visualization of cytoplasmic CFP-SKL (localizing to peroxisomes) or direct monitoring of MS2 loop transcripts with fluorescently tagged MS2 coat protein. Red, yellow and blue circles represent fluorophores used for visualization. (B) Constitutive recruitment of the transcriptional activator VP16 induced production of RNA (top, mKate2-MCP) and the encoded SKL-tagged CFP protein (bottom), which localizes to cytoplasmic peroxisomes. CFP-LacI was included as an array marker (bottom). (C) Constitutive recruitment of VP16 induced recruitment of RNA polymerase II to the array. RNA Pol II was labeled with GFP, RNA with tagRFP-MCP, the (mock) effector with the far-red fluorophore iRFP713. For each condition, 12 images were recorded. Scale bars: 5  $\mu$ m. Magnifications (2 $\times$ ) of the boxed areas in B and C are shown in the top left corner of each image. (D) Association kinetics of PHR-VP16 with CIBN-TetR tethered to the *tetO* sites of the gene array. Averaged experimental data (dark gray lines), fits (black lines) and standard deviations (light gray areas) are shown ( $n=20$ ). The CIBN construct was tagged with tagRFP-T to locate the array without triggering PHR binding. The PHR construct was labeled with YFP for simultaneous recruitment and visualization. (E) Dissociation kinetics of the PHR-VP16 and CIBN-TetR complex ( $n=13$ ). Plot coloring as in panel D. The PHR construct was tagged with mCherry to visualize its dissociation without triggering its interaction with CIBN.

targets are affected with respect to their acetylation state (Choudhary et al., 2009). Those effects also influence the cell cycle, which we assessed in the U2OS cell line studied here by fluorescence-activated cell sorting (FACS). The fraction of cells in S phase was reduced by about 17% with a corresponding increase of the G1 fraction upon SAHA treatment. Thus, SAHA induces other effects than histone hyperacetylation that might also contribute to changes of the transcription activation kinetics.

The produced reporter RNA was not homogeneously distributed across the array (Fig. 3A, insets), suggesting that activated transcription sites are clustered and regulated together. The size of the reporter array remained unchanged within the first 50 min after PHR-YFP-VP16 recruitment as measured on the microscopy images (Fig. 3B, bottom). Thus, the global chromatin decondensation on the  $\mu$ m scale that has been observed previously (Janicki et al., 2004; Rafalska-Metcalf et al., 2010) was not a pre-requisite for PHR-YFP-

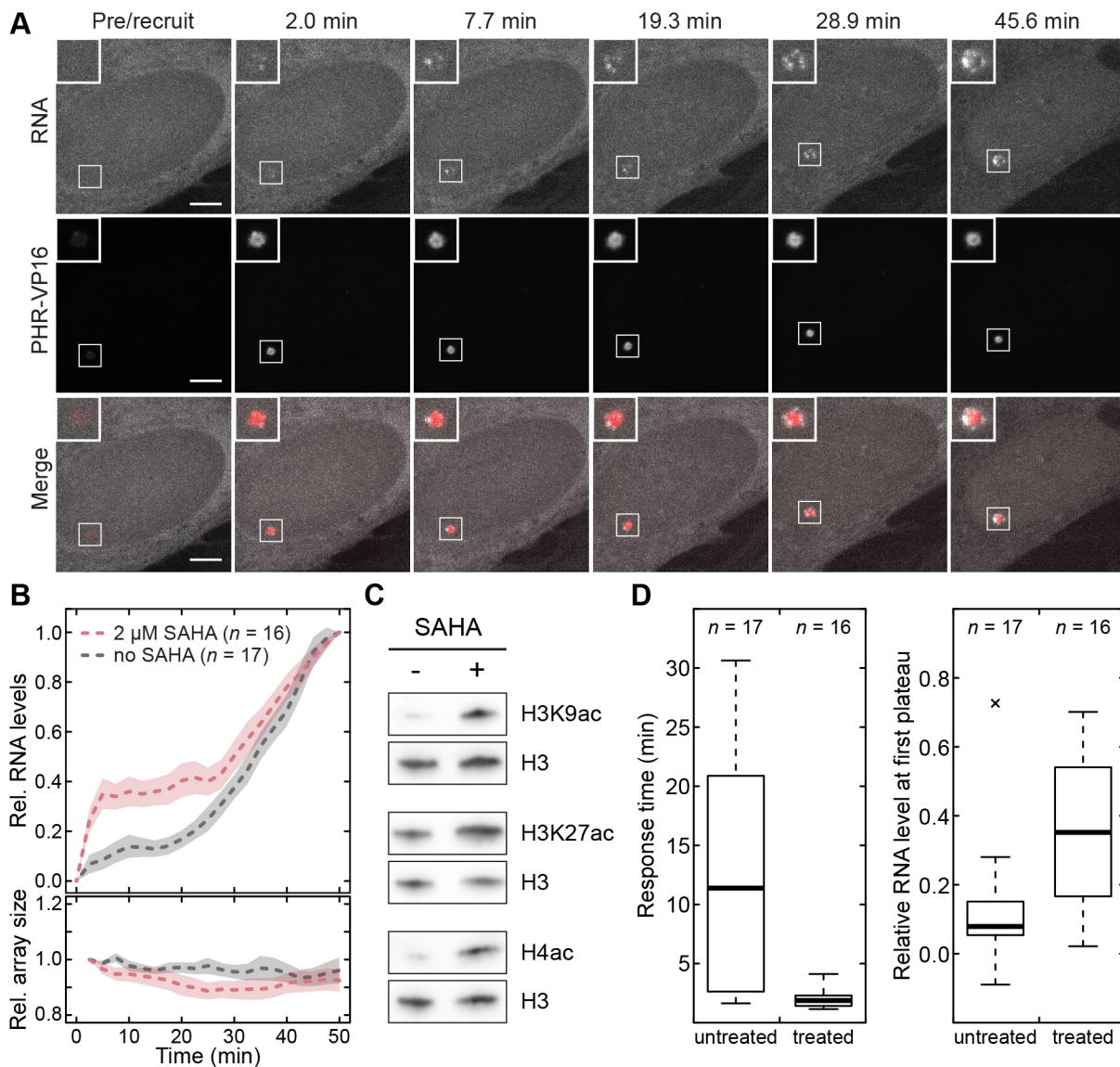


**Fig. 3. BLInCR resolves the early kinetics of the transcription activation process.** (A) Time series of VP16-induced transcription. Top: RNA production visualized by labeled MS2 coat protein (mKate2-MCP). Middle: PHR-VP16 (labeled with YFP) was continuously present at the array during imaging. Bottom: Merged images. Scale bars: 5  $\mu$ m. Magnifications (2 $\times$ ) of the boxed areas are shown in the top left corner of each image. (B) Top: BLInCR-induced transcription with (red) and without (gray) SAHA treatment occurred with an early and a late activation phase. The early response was more pronounced in cells pre-treated with SAHA overnight (red). Depicted are experimental averages (dashed lines) and standard errors of the mean (shaded areas). Bottom: Relative size of the reporter gene array over time as measured on the microscopy images. (C) Western blot of cells treated with (+) and without (–) SAHA. Treatment with SAHA (2  $\mu$ M) for 24 h led to an increase of pre-existing histone acetylation. (D) Cell-to-cell heterogeneity of response times (left) and relative RNA levels (right) in treated and untreated cells. Response times correspond to the time points at which first transcripts were detectable. Relative RNA levels were measured at the point of inflection, i.e. at the first plateau between early and late transcription.

VP16-mediated activation, but might rather occur downstream of transcription initiation (Fig. S1C). This conclusion is in line with other studies showing that decondensation is not required for transcription (Carpenter et al., 2005; Tumber et al., 1999), suggesting that both processes can occur independently from each other. The transcriptional response to recruitment of VP16 was heterogeneous among cells. Without treatment, the response time, after which transcripts were first detectable, varied from <2 min to >30 min, whereas it was always <5 min in SAHA-treated cells (Fig. 3D, left). In addition, the extent of early transcription as estimated from the level of the first plateau at 9–12 min (see Fig. 3B) varied greatly for both treated and untreated cells (Fig. 3D, right), and heterogeneity was also observed among constitutively activated

cells (Fig. S1A,B). This heterogeneity might reflect differences in epigenetic promoter signals and other chromatin features.

**Modeling of transcription activation kinetics**

To investigate the transcription activation mechanism, we analyzed the activation kinetics measured for treated and untreated cells (Fig. 3B) according to the theoretical framework described in Materials and Methods. In a comparison of different models, we found that a previously derived two-state model (Shahrezaei and Swain, 2008) did not fit the early kinetics observed here (Fig. 4A, left). This model has recently been found to describe the reactivation kinetics of a single-copy reporter that was silenced by recruitment of a histone deacetylase beforehand (Bintu et al., 2016). In contrast, a

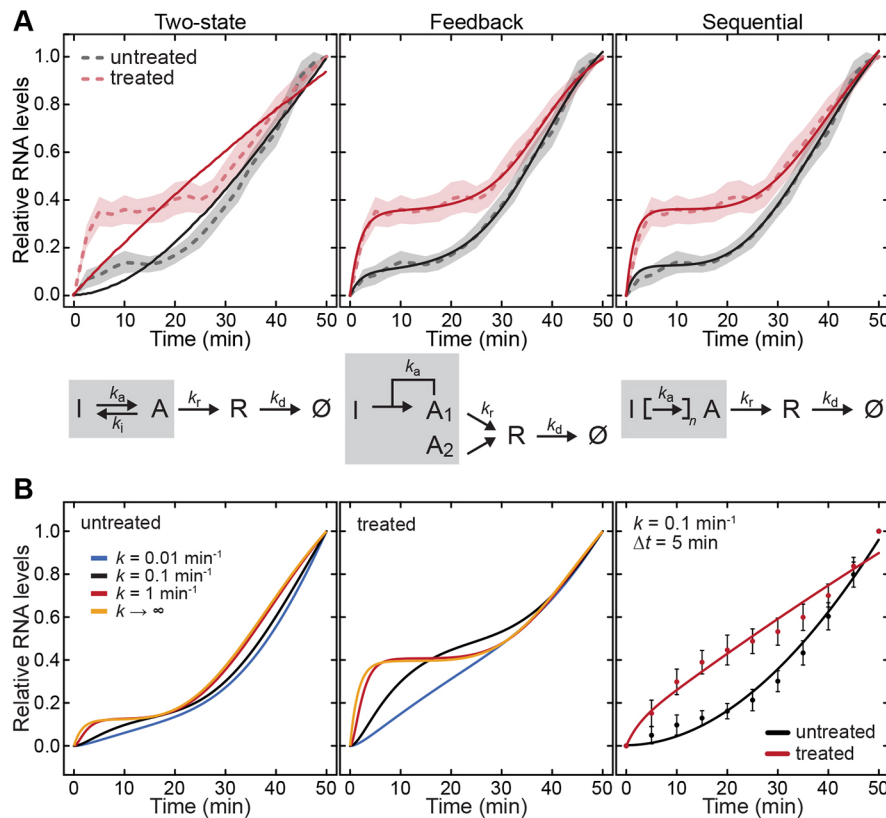


**Fig. 4. Kinetic models of transcription activation.** (A) The experimentally determined activation kinetics were fitted with three different kinetic models: a two-state model, a model including positive feedback, and a sequential activation model (from left to right). The biphasic activation kinetics were reproduced with both the feedback model and the sequential model but not with the two-state model. The parameters  $k_a$ ,  $k_i$ ,  $k_r$  and  $k_d$  denote the rates for activation, silencing, RNA transcription and dissipation of RNA transcripts at the gene array, respectively.  $A$ ,  $A_1$  and  $A_2$  are active states,  $I$  is the inactive state;  $R$  and  $\emptyset$  denote RNA transcription and dissipation, respectively. Fitted parameters are given in Table S4. (B) Influence of recruitment speed on the resulting activation kinetics. The sequential model including an additional initial recruitment step with rate  $k$  was used as a proxy for the expected experimental data. Slow recruitment ( $k \leq 0.1 \text{ min}^{-1}$ ) in combination with moderately fast RNA detection would yield data points that could also be fitted with the two-state model (right plot, with error bars reflecting the experimentally measured ones).

model with the same number of parameters that included positive feedback and a fraction of promoters that acted as independent transcription units fitted the data well (Fig. 4A, center). Positive feedback could originate from spatial interactions among cooperatively transcribed reporter genes (Li et al., 2012; Papantonis and Cook, 2013) and might include the transcription-induced relocalization of promoters during the activation process (Therizols et al., 2014). A third model, which represents the activation process as a series of multiple sequential reaction steps with the same transition rate, also yielded a good but slightly worse fit (Fig. 4A, right). These steps might represent nucleosome repositioning events (Boeger et al., 2008; Nocetti and Whitehouse, 2016), histone modification reactions as well as the recruitment of different components of the transcription machinery. Fitted parameters for the different models are listed in Table S4. Both the feedback and the sequential model predict a rate of  $k_d \sim 0.5 - 0.6 \text{ min}^{-1}$  for the loss of transcripts from the gene array. Thus, RNA molecules dissociate relatively quickly after synthesis.

To assess the influence of the recruitment speed of the activator on the observed activation kinetics we conducted simulations for different recruitment rates (Fig. 4B). To this end, we used the sequential model that serves as a proxy for the experimental data as shown above. Slow recruitment of the activator ( $k \leq 0.1 \text{ min}^{-1}$ , black and blue lines in Fig. 4B) was able to mask the early activation phase. In contrast, fast recruitment ( $k > 1 \text{ min}^{-1}$ , red and yellow lines) with rates similar to those achieved by BLInCR ( $k > 10 \text{ min}^{-1}$  and  $\tau_{1/2} \sim 12 \text{ s}$ , Table S2) was able to resolve both activation phases. Accordingly, the early activation phase might not be visible when using tamoxifen ( $k \sim 0.04 \text{ min}^{-1}$ ,  $\tau_{1/2} \sim 17 \text{ min}$ ; Rafalska-Metcalf et al., 2010) or doxycycline ( $k \sim 0.4 \text{ min}^{-1}$ ,  $\tau_{1/2} \sim 100 \text{ s}$ ; Normanno et al., 2015) to recruit transcriptional activators present at low concentrations. Slow recruitment in combination with moderately fast RNA detection (e.g. every 5 min) would yield data that can be fitted with the two-state model

(Fig. 4B, right). Thus, both fast recruitment of the activator and fast readout of RNA production are crucial to resolve the biphasic activation kinetics and, thereby, distinguish between different activation models.

**Persistence of transcriptional activity**

We next asked if transcriptional activity persists after removal of the activating stimulus (Fig. 5A). Such persistence might, for example, arise from activating histone modifications that keep the reporter array in a permissive state (Ng et al., 2003; Zhang et al., 2015). When we analyzed the RNA signal at the gene array during and after VP16 recruitment (Fig. 5B), we found that RNA production was readily detected upon VP16 binding and decreased upon VP16 dissociation in the absence of blue light (Fig. 5C). As expected, the reporter could be reactivated 40 min after the first activation phase (Fig. 5C). Accordingly, we conclude that transcriptional activity of the gene array requires continuous recruitment of an activator. To validate these findings, we used real-time quantitative PCR to follow the total amount of reporter RNA in cells that had been illuminated for 50 min or 3 h. Total RNA levels should increase over time and reach a plateau if transcriptional activity persists and should decrease over time otherwise (Fig. 5A). For both pulse durations, RNA levels decreased after blue light had been switched off (Fig. 5D), supporting the conclusion that most of the transcriptional activity is lost when VP16 is removed.

**DISCUSSION**

The BLInCR method presented here can rapidly and precisely trigger light-induced recruitment of transcription regulators to genomic loci in single living cells to measure the RNA output with high temporal resolution. It combines the capability of plant-based optogenetic systems for transcriptional control (see, e.g. Konermann et al., 2013; Motta-Mena et al., 2014; Niopek et al., 2014; Polstein and Gersbach, 2015) with the power of real-time microscopy readouts (see, e.g.

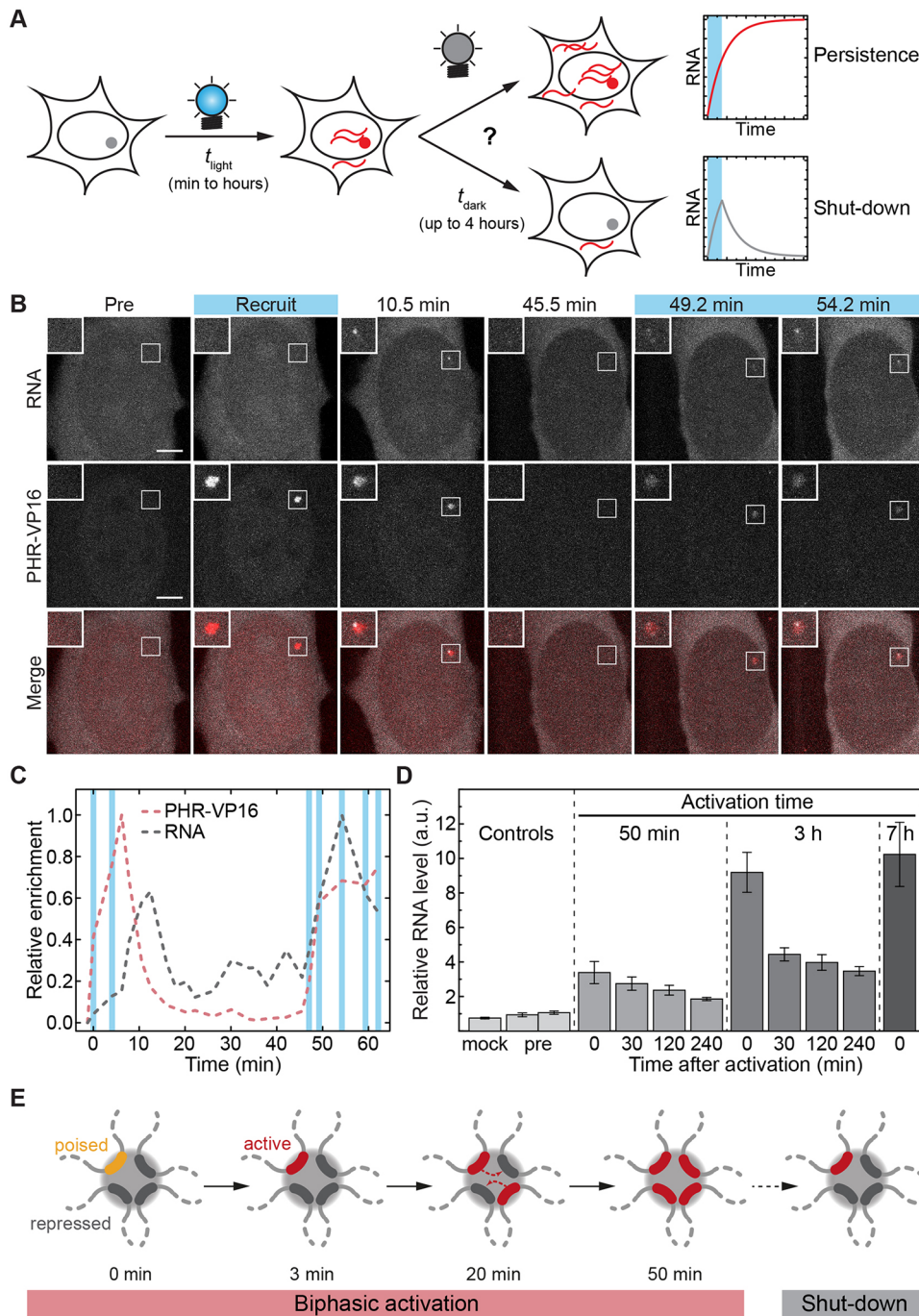


**Fig. 5. Persistence of the activated state.** (A) Scheme for the presence or absence of memory. If the activated state persists, the genes of the reporter array remain associated with nascent reporter RNA, and the total amount of cellular reporter RNA increases after light has been switched off (upwards pointing arrow). In the alternative model, nascent reporter RNA dissociates from array genes and the total amount of cellular reporter RNA decreases when the initial activator has dissociated from the promoter (downwards pointing arrow). (B) Transcription response to pulsed recruitment of VP16. Top row, RNA; middle row, PHR-VP16; bottom row, merged images. The increase and decrease of RNA levels following activator binding and dissociation indicates that the active state did not persist in the absence of VP16. PHR-VP16 was labeled with far-red iRFP713 and RNA was visualized with tagRFP-MCP, so that both can be visualized without triggering recruitment of PHR-VP16. One cell (out of 11) is displayed as an example. Scale bars: 5  $\mu$ m. (C) Quantification of the integrated signal at the gene array from the images shown in B. Shaded areas represent pulses of blue light. (D) Time course of total levels of reporter RNA in the sample after induction. Cells were illuminated with blue light for 50 min, 3 h or 7 h and the amount of reporter RNA was quantified by RT-qPCR at the indicated time points. Controls show RNA levels for mock transfected sample (PHR without VP16) and for samples before light induction. RNA levels decayed after light had been switched off. Notice that, in this assay, the total amount of cellular reporter RNA was measured as opposed to quantification of RNA levels at the reporter gene array in the analysis based on fluorescence microscopy shown in C. (E) Model for the biphasic transcriptional activation kinetics and the reversibility of the activated state observed here by using BLInCR. A fraction of poised promoters is initially present and activated within  $\sim$ 3 min. Maximum RNA accumulation at genes within the array requires about 50 min. After loss of the activator, RNA production decays within minutes.

Janicki et al., 2004). In this manner, cellular function can be dissected at subcellular resolution over time. Our approach can be easily adapted to study the activities of other PHR-fused effectors within any nuclear subcompartment that can be marked by CIBN-fused targeting factors. While the present study applied only confocal fluorescence microscopy imaging, BLInCR is compatible with several fluorescence microscopy-based techniques, such as wide-field microscopy with regular filter sets, super-resolution microscopy, single-particle tracking and other approaches for mobility imaging. We have focused here on the measurement of RNA production by using fluorescent MS2 coat proteins as a prototypical functional readout in order to monitor cellular processes in real-time. Further, we exploited the high temporal resolution of BLInCR to distinguish between conceptually different models for

transcriptional activation. Kinetic modeling revealed that even strong transcriptional activators, such as VP16, cannot readily activate an entire gene cluster in one step (Fig. 5E). Rather, full activity is only reached after a pronounced maturation phase, which might allow actively transcribed genes to contact and activate other promoters in close spatial proximity (Cremer et al., 2015; Papanonis and Cook, 2013). Notably, a similar mechanism has been proposed to explain the function of actively transcribed enhancers (Li et al., 2016). Furthermore, we found that the lifetime of the activated state is limited, suggesting that even a cluster containing several active genes requires the continuous presence of transcriptional activators to maintain its activity. We anticipate that BLInCR will facilitate the study of the dynamic regulation of transcription and other nuclear processes for which the induction kinetics as well as the persistence

of the output signal are crucial parameters to understand the underlying molecular mechanisms.

## MATERIALS AND METHODS

No statistical methods were used to pre-determine sample size. The experiments were not randomized and the investigators were not blinded to allocation during experiments and outcome assessment.

### Plasmids

Effector and localizer plasmids were constructed on the basis of sequences coding for the PHR domain of CRY2 and the CIBN domain of CIB1. pCRY2PHR-mCherryN1 and pCIBN(deltaNLS)-pmGFP, as described by Kennedy et al., 2010, were obtained from Addgene (plasmid number 26866 and number 26867). LacI and TetR constructs are based on the fluorescently tagged proteins described by Lau et al., 2003 and Pankert et al., 2017. Human GCN5 was cloned from pAdEasy Flag GCN5 (Lerin et al., 2006) (Addgene plasmid number 14106). The near-infrared fluorescent protein iRFP713 was from piRFP (Filonov et al., 2011) (Addgene plasmid number 131857). The NLS used in some of the BLInCR constructs (Table S1) is the peptide PKKKRKY from the SV40 large T-antigen (Kalderson et al., 1984), and was inserted by PCR. The MCP was derived from previously described vectors (Auslander et al., 2012; Pankert et al., 2017). Other human plasmids were derived from previously described vectors containing sequences coding for TRF1 (also known as TERF1; Chung et al., 2011), TRF2 (also known as TERF2) (Jegou et al., 2009), PML splicing isoform III (Jegou et al., 2009), Nucleolin (Caudron-Herger et al., 2015), Lamin B1 (Muller-Ott et al., 2014) the viral transactivator VP16 (also known as UL48) (Günther et al., 2013) and GFP-tagged RNA polymerase II (GFP-Pol II) (Sugaya et al., 2000). Plasmids associated with this study are available at the Addgene plasmid repository.

### Cell culture and transfection

The U2OS 2-6-3 cell line has been described previously (Janicki et al., 2004) and was kindly provided by Susan Janicki and David Spector. Cells were cultured in DMEM medium containing 1 g l<sup>-1</sup> glucose, supplemented with 10% doxycycline-free fetal bovine serum, 1× penicillin/streptomycin and 2 mM stable glutamine. For live cell experiments, cells were seeded in matrigel-coated (1:100 in serum-free medium for at least 30 min at room temperature) chamber slides (Cellview; Greiner Bio-One, Kremsmünster, Austria) and cells were seeded on glass coverslips or in 4-well culture inserts (Ibidi, Martinsried, Germany) for immunofluorescence and RNA FISH. Cells were transfected with the appropriate constructs using Effectene (Qiagen, Germany) or Xtreme Gene 9 transfection reagent (Roche) in case of subsequent RNA isolation (for RT-qPCR or RNA-seq). Medium was changed 4 h after transfection, and 2 μM SAHA (Millipore) was added to the fresh medium if applicable. The FACS analysis of the cell cycle distribution was conducted as described previously (Osterwald et al., 2015).

### Fluorescence microscopy and image processing

Cells were kept in the dark overnight and mounted on a Leica TCS SP5 confocal microscope equipped with a HCX PL APO lambda blue 63×/1.4 NA oil immersion objective. A red flashlight was used to avoid premature exposure to blue light. The following excitation and emission wavelengths were used: CFP (405 nm/415–475 nm), GFP/YFP (488 nm/500–550 nm), tagRFP/tagRFP-T (561 nm/575–630 nm), mCherry/mKate2 (594 nm/605–750 nm), iRFP713 (633 nm/645–780 nm). Images were acquired as described below for the different experiments. Image analysis was done using the Fiji distribution (Schindelin et al., 2012) of ImageJ (Schneider et al., 2012). The enrichment  $E(t)$  of a given protein at the *tetO* or *lacO* arrays was calculated from single images or the maximum intensity projections of image stacks. To quantify enrichments, the intensity difference between the array region ( $I_{array}$ ) and the nuclear reference region ( $I_{nuc}$ ) was computed for each time point:

$$E(t) = I_{array}(t) - I_{nuc}(t). \quad (1)$$

The nuclear reference region was selected to be close to the array region to account for uneven illumination of the cell if necessary, but outside of nucleoli, which generally showed some depletion of the constructs. To correct for bleaching, the decay of the mean intensity difference at the nuclear reference region and a background region outside of the cell  $I_{nuc}(t)$

$-I_{background}(t)$  was fitted with a single exponential term  $a e^{-k \cdot t}$ . The enrichment  $E$  at the array was then calculated as the intensity difference between array and nuclear reference region divided by the bleach contribution  $e^{-k \cdot t}$ , which was assumed to be the same for the array and the nucleus:

$$E(t) = (I_{array}(t) - I_{nuc}(t)) / e^{-k \cdot t}. \quad (2)$$

### BLInCR recruitment kinetics

U2OS 2-6-3 cells were transfected with CIBN-TetR-tagRFP-T and a PHR-YFP construct (i.e. PHR-YFP-VP16, PHR-YFP-NLS or PHR-YFP-hGCN5). Transfected cells and reporter arrays were identified in the tagRFP-T channel. Subsequently, an image series of 400 frames with 256×256 pixel (px) images was recorded in the YFP channel at a scan speed of 1400 Hz corresponding to 204.3 ms per image and a total of 82 s. Excitation of YFP caused optogenetic switching, resulting in accumulation of the respective PHR-YFP construct at the CIBN site, i.e. the array seen in the tagRFP-T channel (Fig. S4A). To quantitatively analyze the enrichment of PHR-YFP constructs at the gene array, a maximum intensity projection was used to select the array region (diameter: ~15 px) and a nuclear reference region (diameter: 30 px) at which the mean fluorescence intensities were measured (Fig. S4A) to compute  $E(t)$  as described above. For PHR-YFP accumulation, all curves could be fitted well with a model containing two exponentials:

$$E(t) = a - b \cdot \exp(-k_1 \cdot t) - c \cdot \exp(-k_2 \cdot t). \quad (3)$$

This equation describes a reaction model with two parallel first-order reactions to the same product (Steinfeld et al., 1989). The characteristic rates  $k_1$  and  $k_2$  were fitted globally, whereas the plateau value  $a$  and the contributions of the two reactions  $b$  and  $c$  were fitted for each single curve. From the fit, the characteristic recruitment time  $\tau_{1/2}$  was calculated as given below:

$$E(\tau_{1/2}) = E(0) + \frac{E(\infty) - E(0)}{2}. \quad (4)$$

$E(0)$  and  $E(\infty)$  were obtained as fitted parameters and the plateau value  $E(\infty)=a$  was used for normalization according to  $E_{norm}(t)=E(t)/a$ . Finally, all normalized curves and fits were averaged, yielding curves as in Fig. 2D and Fig. S4B. Cells that moved in *z*-direction leading to fluctuations in the enrichment curves as well as cells with very low YFP signal and bad signal-to-noise ratio were excluded from the analysis.

### BLInCR dissociation kinetics

U2OS 2-6-3 cells were transfected with CIBN-TetR, GFP-LacI and a PHR-mCherry construct, i.e. PHR-mCherry-VP16 or PHR-mCherry-NLS. Transfected cells were identified in the mCherry channel and a pre-recruitment stack (seven slices with  $\Delta z=0.5 \mu\text{m}$ , 2× line average, 512×512 px, 400 Hz scan speed) was recorded. To recruit the PHR-mCherry constructs to the array, two stacks were recorded in the GFP channel corresponding to 38 s illumination with blue light. The first post-recruitment stack was recorded in the mCherry channel immediately afterwards and represents the time point  $t=0$  s. Subsequent stacks were acquired every ~30 s for the first ~5 min and then at longer intervals for about 30 min (Fig. S4C). The focus was re-adjusted if necessary.

To quantify the reversibility kinetics, the *z*-stacks for each time point were registered using the StackReg plugin (Thevenaz et al., 1998). For each time point, a maximum projection of the registered *z*-slices was made, resulting in a time series of maximum projections. Generally, cell shapes changed considerably over the 30 min acquisition time, preventing registration of the time series. Consequently, the array region (diameter: 20–40 px) and a nuclear reference region (diameter: 60 px) were manually selected for each time point and mean fluorescence intensities were measured (Fig. S4C). Importantly, the sizes of the regions were kept constant over all images of one time series.

All  $E(t)$  curves could be fitted well with a single exponential with a time-dependent (i.e. concentration-dependent) reaction rate similar to the model proposed by Sing et al. (2014):

$$E(t) = a \cdot \exp(-k \cdot t^{m'}) + c. \quad (5)$$

From the fit, the characteristic half-life  $t_{1/2}$  was calculated:

$$E(t_{1/2}) = E(0) + \frac{E(0) - E(\infty)}{2}. \quad (6)$$

$E(0)$  and  $E(\infty)$  were calculated from the fit and used for normalization:

$$E_{\text{norm}}(t) = \frac{E(t) - E(\infty)}{E(0) - E(\infty)}. \quad (7)$$

The normalized curves were averaged to yield the data shown in Fig. 2E and Fig. S4D.

### Light-induced transcription activation

U2OS 2–6–3 cells were transfected with mKate2-MCP for RNA readout, CIBN-TetR as recruitment platform, CFP-LacI as array marker and PHR-YFP-VP16 for recruitment to CIBN-TetR and subsequent transcriptional activation. Image acquisition was similar to that used for the reversibility kinetics as described (Fig. S4C) except for an additional third scan (CFP) and a 4× line average instead of 2×. After constitutive recruitment with a blue LED overnight, four slices ( $\Delta z=0.5 \mu\text{m}$ ) were recorded. For the time series, the number of slices recorded was between five and eight ( $\Delta z=0.5 \mu\text{m}$ ), depending on cell size and shape. This was done to ensure that the gene array was located within the recorded range since it cannot be seen in the pre-recruitment image. For the first stack (pre-recruit/recruit), the channels were switched between stacks, with the red channel (mKate2) being recorded first (yielding the reference image for mKate2-MCP before VP16 recruitment), then the YFP channel and last the CFP channel. For all subsequent stacks (one stack every 2–4 min) as well as after constitutive activation, all three channels were recorded sequentially using the ‘between lines’ mode. Hence, different color images did not need to be registered with respect to one another. However, different z-slices had to be registered since the recording of an entire image stack with three colors lasted longer than 1 min, so that movement of the cell was occasionally observed. The different z-slices were transformed to RGB stacks and then registered to one of the central slices on the basis of the YFP channel using the TurboReg (Thevenaz et al., 1998) plugin.

To quantify the RNA amount at the array, maximum intensity projections were made for each time point resulting in a stack of three projections of maximum intensity (mKate2, YFP and CFP). The quantification was also done manually for each time point as described above for the reversibility kinetics. Note that the region of interest around the array was selected in the YFP and/or CFP channel and was kept at the same size (diameter: 20–40 px) across all time points for a single cell. The  $E(t)$  curves for RNA/mKate2-MCP enrichment at the array were calculated as described above, normalized to the enrichment values before and after 50 min of VP16 recruitment, and averaged (Fig. 3B). The average curve was fitted by using a simple two-state model, a model assuming positive feedback or a sequential activation model (Fig. 4A) as described below.

To calculate the RNA enrichment values at the first plateau (Fig. 3D), the inflection points were calculated from the fit of the average curves (feedback model) of untreated and treated cells. The time course of array sizes was determined from the PHR-YFP-VP16 or the CFP-LacI signal with ImageJ. The local area around the array (diameter: 60 px/3.2  $\mu\text{m}$ ) was selected and converted to a binary image of the array by using Otsu’s method (Otsu, 1979) for thresholding. The measured array sizes at each time point were normalized to the array size at  $t=2.5$  min to assure that PHR-YFP-VP16 was fully recruited.

To compare RNA levels after constitutive activation, cells were transfected with PHR-YFP or PHR-YFP-VP16 and CFP-LacI as well as CIBN-TetR, exposed to a blue LED overnight or via expression of a co-transfected GFP-TetR-VP16 fusion protein (Fig. S1). CLSM imaging was conducted with the same laser intensities on the same day. The enrichment of fluorescence intensity of RNA/mKate2-MCP was calculated from the background-corrected intensities and the size of the array area  $A_{\text{array}}$  according to

$$E = (I_{\text{array}} - I_{\text{nuc}}) \cdot A_{\text{array}}. \quad (8)$$

### BLInCR transcription activation and reversibility

To test the reversibility of transcription activation, cells were transfected with tagRFP-MCP for RNA detection, CFP-LacI as array marker as well as CIBN-TetR and PHR-iRFP713-VP16 for light-induced recruitment of VP16 to the reporter array. In this manner, both RNA and VP16 can be separated spectrally, and monitored without triggering PHR recruitment. The imaging parameters

size, speed and line averaging were the same as for the light-induced transcription activation described above. Prior to recruitment and activation, a two-color stack (iRFP713 and tagRFP, sequential scan in ‘between lines’ mode) was recorded, ensuring that neither VP16 nor RNA were detectable at the gene array. For light-induced recruitment of VP16, two three-color stacks (iRFP713, tagRFP and CFP, sequential scan in ‘between lines’ mode) were recorded and the beginning of the first stack is the time point  $t=0$  s. Each stack acquisition exposed the cells to blue light for 78 s, and both stacks were recorded ~3 min apart. Subsequently, two-color stacks (iRFP713 and tagRFP) were recorded every 2–4 min to monitor PHR-iRFP713-VP16 dissociation, and tagRFP-MCP accumulation and dissociation from the array. After 30–40 min, PHR-iRFP713-VP16 was recruited again by switching back to three-color imaging (iRFP713, tagRFP and CFP). RNA and PHR-iRFP713-VP16 quantification at the array and bleach correction were performed as described above. The maximum enrichment value and the enrichment value before VP16 recruitment  $E(0)$  were used for normalization.

### FISH and immunofluorescence

RNA production from the reporter gene array was analyzed by RNA fluorescence in situ hybridization (FISH). Cells were seeded on cover slips and transfected with CIBN-TetR, CFP-LacI and PHR-YFP or PHR-YFP-VP16 as described above. After illumination with a blue LED overnight, cells were permeabilized on ice with CSK buffer (100 mM NaCl, 300 mM sucrose, 3 mM  $\text{MgCl}_2$ , 10 mM PIPES, 0.5% Triton X-100) containing 10 mM vanadyl ribonucleoside complex (VRC, New England Biolabs) for 5 min. Further processing was done at room temperature unless noted otherwise: Cells were washed once with PBS, fixed with paraformaldehyde (12 min) and washed again with PBS. Subsequently, they were incubated with 70%, 85% and 100% ethanol (3 min each) and air-dried. For MS2 stem loop RNA detection, 50 ng of the 5'-Atto-565-labeled antisense probe 5'-GTC GAC CTG CAG ACA TGG GTG ATC CTC ATG TTT TCT AGG CAA TTA-3' (Goodier et al., 2010) per slide were mixed with 10  $\mu\text{g}$  salmon sperm DNA and 5  $\mu\text{l}$  formamide. The mixture was heated to 37°C for 10 min and 74°C for 7 min before 5  $\mu\text{l}$  hybridization buffer (0.6 M NaCl and 60 mM trisodium citrate, pH 7.0, 20% dextran sulfate and 2 mg/ml BSA) and 10 mM VRC were added to a total volume of 11  $\mu\text{l}$ . After hybridization overnight at 37°C, cover slips were washed as follows: twice with 2× SSC (0.3 M NaCl, 30 mM trisodium citrate, pH 7.0) supplemented with 50% formamide (15 min), once with 0.2× SSC/0.1% Tween (10 min, 40°C), once with 2× SSC (5 min), and once with PBS. Subsequently, YFP was visualized by immunofluorescence staining with an anti-GFP antibody since the fluorophore was destroyed during RNA-FISH. Cells were permeabilized with 0.1% ice-cold Triton X-100/PBS (5 min), washed once with PBS (5 min) and blocked with 10% goat serum in PBS for 30 min. The samples were incubated with the respective primary antibody (in 5% goat serum/PBS; see Table S5 for antibody details) for 1–2 h or overnight at 4°C. After washing three times with PBS supplemented with 0.002% NP40, samples were incubated with an Alexa-Fluor-488-coupled secondary antibody (Life Technologies) for 45 min and washed with PBS (3×5 min). Lastly, the slides were rinsed with water, 75% ethanol and 100% ethanol before mounting them with ProLong gold antifade mountant including DAPI (Life Technologies). For immunofluorescence staining of RNA polymerase II and H3K9ac (Figs S2 and S5), cells were fixed after 19–24 h exposure to blue light (LED) using 4% paraformaldehyde (7 min) and washed three times with PBS. Next, cells were permeabilized and processed as described above. The primary antibody used against H3K9ac was from ActiveMotif (catalog number 139917). The secondary antibody was Alexa-Fluor-568-coupled (Fig. S5A,B) or an Alexa-Fluor-633-coupled (Fig. S5C) anti-rabbit IgG antibody (Life Technologies). For immunofluorescence staining of RNA polymerase II phosphorylated at serine 2 or 5, the primary antibody clones 3E10 and 3E8 were used (ActiveMotif, catalog numbers 161083 and 61085, respectively). The secondary antibody was Alexa-Fluor-647-coupled (Life Technologies). Additional details on the antibodies used is given in Table S5.

### Histone extraction and western blotting

U2OS 2–6–3 cells were cultured with 2  $\mu\text{M}$  SAHA (Millipore, 1:1000 from 2 mM stock solution in ethanol) or 1:1000 ethanol for 24 h. Histones were extracted from  $\sim 1 \times 10^6$  cells using 0.25 M HCl as described previously (Shector et al., 2007; Villar-Garea, 2008), separated by electrophoresis on a

precast 4–20% polyacrylamide gel (Bio-Rad) and blotted semi-dryly onto a nitrocellulose membrane. After blocking in Tris-buffered saline (TBS) with 5% milk, modified histones were detected with primary antibodies against H3K27ac, H3K9ac (both diluted in TBS with 1% BSA) and H4ac (in TBS with 3% milk) and HRP-linked anti-rabbit IgG (in TBS with 5% milk). Bands were detected by chemoluminescence using clarity western ECL substrate (Bio-Rad). After stripping the membranes with stripping buffer (Carl Roth), total H3 levels were detected with an antibody against H3 (in TBS with 1% BSA) and a secondary HRP-linked antibody against mouse IgG (in TBS with 5% milk). Additional information on the used antibodies is found in Table S5.

**RNA sequencing**

For RNA sequencing (RNA-seq), RNA ( $\geq 200$  nt) was isolated with the NucleoSpin RNA Plus kit (Macherey-Nagel), digested by DNase I (Promega) for 30 min at 37°C and depleted from rRNA with RiboZero (Illumina). Finally, directional cDNA synthesis and sequencing library preparation was conducted according to the NEBNext Ultra II Directional RNA Library Prep Kit (NEB). All libraries were sequenced as 50 bp single-end reads on an Illumina HiSeq 4000 system. Reads were mapped to the sequences of the respective transfected constructs and the inserted reporter using bowtie (Langmead et al., 2009). Subsequently, the remaining reads were mapped to the hg38 assembly of the human genome using STAR (Dobin et al., 2013). Normalization and differential expression analysis were performed using DESeq2 (Love et al., 2014).

**RT-qPCR**

For RT-qPCR, RNA was isolated and DNA was digested as described above for RNA-seq, cDNA was synthesized using Superscript IV reverse transcriptase (ThermoFisher, USA) and RNA was digested using RNase H. The qPCR reaction was performed using the SYBR Green mix (Applied Biosystems, CA) and primers specific for the CFP-SKL reporter (fwd: 5'-GTC CGG ACT CAG ATC TCG A-3' and rev: 5'-TTC AAA GCT TGG ACT GCA GG-3', designed with Primer3; Untergasser et al., 2012) with the following program: 10 min, 95°C and 40 cycles of 1 min, 60°C. RNA was quantified using a standard dilution and normalized to average “pre” levels before illumination. A non-transfected sample (‘mock’) was included as a control.

**Theoretical framework for kinetics analysis**

**Two-state kinetic model of transcriptional activation**

Curves for the relative RNA levels in Fig. 3B were fitted with a two-state model according to the scheme depicted below the plot. The differential equations for the activated state ( $A$ ) and the RNA level ( $R$ ) read

$$\begin{aligned} \frac{dA(t)}{dt} &= [1 - A(t)] \cdot k_a - A(t) \cdot k_i \\ \frac{dR(t)}{dt} &= A(t) \cdot k_r - R(t) \cdot k_d \end{aligned} \tag{9}$$

Here,  $k_a$  and  $k_i$  are the transition rates into the activated and inactive state, respectively.  $k_r$  is the RNA production rate, and  $k_d$  is the RNA dissipation rate from the array. The total number of active and inactive promoters is normalized to 1, so that the initial concentration  $A_0$  can take on values between 0 and 1. The solution for these equations is given by

$$\begin{aligned} A(t) &= A_0 e^{-(k_a+k_i)t} + \frac{k_a}{k_a+k_i} (1 - e^{-(k_a+k_i)t}) \\ R(t) &= k_r \left[ \frac{k_a}{k_d(k_a+k_i)} + \frac{[k_a - A_0(k_a+k_i)]e^{-(k_a+k_i)t}}{(k_a+k_i)(k_a-k_d+k_i)} - \frac{[k_a - A_0k_d]e^{-k_d t}}{k_d(k_a-k_d+k_i)} \right] \end{aligned} \tag{10}$$

The fitted parameters corresponding to the functions in Fig. 4A are listed in Table S4. The decay rate  $k_d$  was set to be equal for untreated and SAHA-treated cells. Furthermore, fits were constrained not to exceed relative RNA levels of 5 a.u. (reached in steady-state at  $t=\infty$ ), reflecting the fact that measured RNA levels remained below this level also for late time points (up to 24 h post-induction).

**Three-state kinetic model with feedback for transcriptional activation**

Curves for the relative RNA levels in Fig. 3B were fitted with a three-state model involving feedback according to the scheme shown below the plot. The differential equations for the activated state ( $A_1$ ) and the RNA level ( $R$ ) read

$$\begin{aligned} \frac{dA_1(t)}{dt} &= [1 - A_1(t) - A_2] \cdot A_1(t) \cdot k_a \\ \frac{dR(t)}{dt} &= [A_1(t) + A_2] \cdot k_r - R(t) \cdot k_d \end{aligned} \tag{11}$$

Here,  $k_a$  is the transition rate into the activated state  $A_1$ , and  $A_2$  is the population residing in the activated state  $A_2$ . Again, the total number of promoters is normalized to 1. The solution for these equations is given by

$$\begin{aligned} A_1(t) &= \frac{C(1 - A_2)}{C + e^{-k_c t}} \\ R(t) &= \frac{C(A_2 - 1)k_r e^{-k_d t}}{k_c + k_d} [{}_2F_1(1, K + 1, K + 2, -C) - e^{-(k_c+k_d)t} {}_2F_1(1, K + 1, K + 2, -C \cdot e^{k_c t})] + \frac{A_2 k_r}{k_d} (1 - e^{-k_d t}) \end{aligned} \tag{12}$$

with the abbreviations

$$C = \frac{A_{1,0}}{1 - A_{1,0} - A_2}, K = \frac{k_d}{(1 - A_2)k_a} \text{ and } k_c = (1 - A_2)k_a. \tag{14}$$

In these equations,  $A_{1,0}$  is the initial population in state  $A_1$ ,  $A_2$  is the (invariant) population in state  $A_2$ , and  ${}_2F_1(a, b, c, x)$  denotes the Gaussian hypergeometric function. The fitted parameters corresponding to the functions shown in Fig. 4A are listed in Table S4. The dissipation rate  $k_d$  was set to be equal for untreated and SAHA-treated cells.

**Sequential model for transcriptional activation**

Curves for the relative RNA levels in Fig. 3B were fitted with a sequential model involving  $n$  sequential reaction steps to transition from the inactive state ( $I=S_0$ ) to the active state ( $A$ ) according to the scheme  $I \rightarrow S_1 \rightarrow S_2 \rightarrow \dots \rightarrow S_{n-1} \rightarrow A$ . Here,  $S_i$  represent intermediate states, in which no RNA is produced. For simplicity, the same rate constant  $k_a$  was chosen for each transition. The differential equations for the individual states ( $I, S_i, A$ ) and the RNA level ( $R$ ) read

$$\begin{aligned} \frac{dI(t)}{dt} &= -k_a \cdot I(t) \\ \frac{dS_i(t)}{dt} &= k_a \cdot (S_{i-1}(t) - S_i(t)) \quad (0 < i < n) \\ \frac{dA(t)}{dt} &= k_a \cdot S_{n-1}(t) \\ \frac{dR(t)}{dt} &= k_r \cdot A(t) - k_d \cdot R(t). \end{aligned} \tag{15}$$

The solutions for  $A(0)=A_0$  and  $I(0)=1-A_0$  are given by

$$\begin{aligned} I(t) &= (1 - A_0) e^{-k_a t} \\ S_i(t) &= \frac{(1 - A_0)(k_a t)^i}{i!} e^{-k_a t} \\ A(t) &= 1 - (1 - A_0) \frac{\Gamma(n, k_a t)}{(n - 1)!} \\ R(t) &= \frac{(1 - A_0)k_r}{k_d(n - 1)!} \left[ \frac{k_a(k_a t)^{n-1}}{k_a - k_d} \left( e^{-k_a t} + \frac{(n - 1) e^{-k_d t}}{((k_a - k_d)t)^{n-1}} \Gamma(n - 1, (k_a - k_d)t) \right) \right. \\ &\quad \left. + (n - 1)! \left( 1 - \left( \frac{k_a}{k_a - k_d} \right)^{n-1} e^{-k_d t} \right) - \Gamma(n, k_a t) \right] \\ &\quad + \frac{A_0 k_r}{k_d} (1 - e^{-k_d t}). \end{aligned} \tag{16}$$

Here,  $A_0$  is the initial population in the active state  $A$ , and  $\Gamma(x, y)$  is the (upper) incomplete Gamma function. The fitted parameters corresponding to the functions in Fig. 4A are listed in Table S4. The decay rate  $k_d$  was set to be equal for untreated and SAHA-treated cells.

**Sequential model with additional recruitment step**

The scheme for the sequential activation model above was extended to explicitly include an additional recruitment step for the transcriptional activator with rate  $k_{rec}$ . In particular, an unbound inactive state ( $U_I$ ) and an unbound active state ( $U_A$ ) were considered, with transitions from  $U_I$  to  $I$  and  $U_A$  to  $A$  that occur with rate  $k_a$ . Thus, the reaction schemes read  $U_I \xrightarrow{k_{rec}} I \rightarrow S_1 \rightarrow S_2 \rightarrow \dots \rightarrow S_{n-1} \rightarrow A$  and  $U_A \xrightarrow{k_{rec}} A$ . In this case, the differential equations for the individual states ( $U_A, U_I, I, S_i, A$ ) and the RNA level ( $R$ ) read

$$\begin{aligned} \frac{dU_I(t)}{dt} &= -k_{rec} \cdot U_I(t) \\ \frac{dI(t)}{dt} &= k_a \cdot (U_I(t) - I(t)) \\ \frac{dS_i(t)}{dt} &= k_a \cdot (S_{i-1}(t) - S_i(t)) \quad (0 < i < n) \quad (17) \\ \frac{dA(t)}{dt} &= k_a \cdot S_{n-1}(t) + k_{rec} \cdot U_A(t) \\ \frac{dR(t)}{dt} &= k_r \cdot A(t) - k_d \cdot R(t). \end{aligned}$$

The solutions for  $U_A(0)=A_0$  and  $U_I(0)=1-A_0$  are given by

$$\begin{aligned} U_I(t) &= (1 - A_0)e^{-k_{rec}t} \\ I(t) &= \frac{(1 - A_0)k_a e^{-k_a t}}{k_{rec} - k_a} (1 - e^{-(k_{rec} - k_a)t}) \\ S_i(t) &= (1 - A_0) \frac{k_{rec} k_a^i}{(k_a - k_{rec})^{i+1}} \left( 1 - \frac{\Gamma(i + 1, (k_a - k_{rec})t)}{i!} \right) e^{-k_{rec}t} \\ A(t) &= A_0 (1 - e^{-k_{rec}t}) \\ &\quad + (1 - A_0) \left( 1 - \left( \frac{k_a}{k_a - k_{rec}} \right)^n \left( 1 - \frac{\Gamma(n, (k_a - k_{rec})t)}{(n - 1)!} \right) e^{-k_{rec}t} - \frac{(k_a t)^{n-1}}{(n - 1)!} e^{-k_a t} - \frac{\Gamma(n - 1, k_a t)}{(n - 2)!} \right) \\ R(t) &= \frac{A_0 k_r}{k_d (k_d - k_{rec})} (k_d (1 - e^{-k_{rec}t}) - k_{rec} (1 - e^{-k_d t})) \\ &\quad + \frac{(1 - A_0) k_r}{k_d} \left( 1 - \frac{\Gamma(n - 1, k_a t)}{(n - 2)!} + \frac{k_d e^{-k_{rec}t}}{k_d - k_{rec}} \left( \frac{k_a}{k_a - k_{rec}} \right)^n \left( \frac{\Gamma(n, (k_a - k_{rec})t)}{(n - 1)!} - 1 \right) \right. \\ &\quad \left. + \frac{k_d e^{-k_d t}}{k_a} \left( \frac{k_a}{k_a - k_d} \right)^n \left( \frac{k_a k_{rec}}{k_d (k_d - k_{rec})} + \left( \frac{k_a}{k_d} - 1 \right) \frac{\Gamma(n - 1, (k_a - k_d)t)}{(n - 2)!} \right) \right. \\ &\quad \left. + \left( 1 - \frac{k_a}{k_d - k_{rec}} \right) \frac{\Gamma(n, (k_a - k_d)t)}{(n - 1)!} \right). \end{aligned} \quad (18)$$

Here,  $\Gamma(x, y)$  is the (upper) incomplete Gamma function. Resulting curves for different recruitment rates  $k_{rec}$  are shown in Fig. 4B.

**Acknowledgements**

We thank Caroline Bauer and Delia Braun (DKFZ) for help, the DKFZ light microscopy and sequencing core facilities for technical support and expertise, and Katharina Müller-Ott (DKFZ) for comments on the manuscript. We are grateful to David Spector (Cold Spring Harbour Laboratory, NY) and Susan Janicki (Wistar Institute, PA) for providing the U2OS 2-6-3 cell line, and Kimihiko Sugaya and Jan Ellenberg (EMBL) for providing the GFP-Pol II plasmid.

**Competing interests**

The authors declare no competing or financial interests.

**Author contributions**

Conceptualization: A.R., F.E., K.R.; Methodology: A.R., F.E., J.T., K.R.; Validation: A.R.; Formal analysis: A.R., F.E., J.T.; Investigation: A.R., F.E., J.T., S.S.; Resources: A.R., F.E., J.T., K.R.; Writing – original draft preparation: A.R., F.E., K.R.; Writing – review & editing: A.R., F.E., K.R.; Visualization: A.R., F.E., K.R.; Supervision: K.R.; Project administration: K.R.; Funding acquisition: K.R.

**Funding**

This work was supported by the Deutsche Forschungsgemeinschaft (DFG grant RI 1283/14-1 to K.R.), the Deutsches Krebsforschungszentrum (DKFZ intramural junior researcher grant to F.E.) and the project ENHANCE within the NCT 3.0 program of the National Center for Tumor Diseases (NCT) Heidelberg.

**Data availability**

RNA sequencing data have been deposited in NCBI's Gene Expression Omnibus and are accessible through GEO accession number GSE103868 (<https://www.ncbi.nlm.nih.gov/geo/query/acc.cgi?acc=GSE103868>).

**Supplementary information**

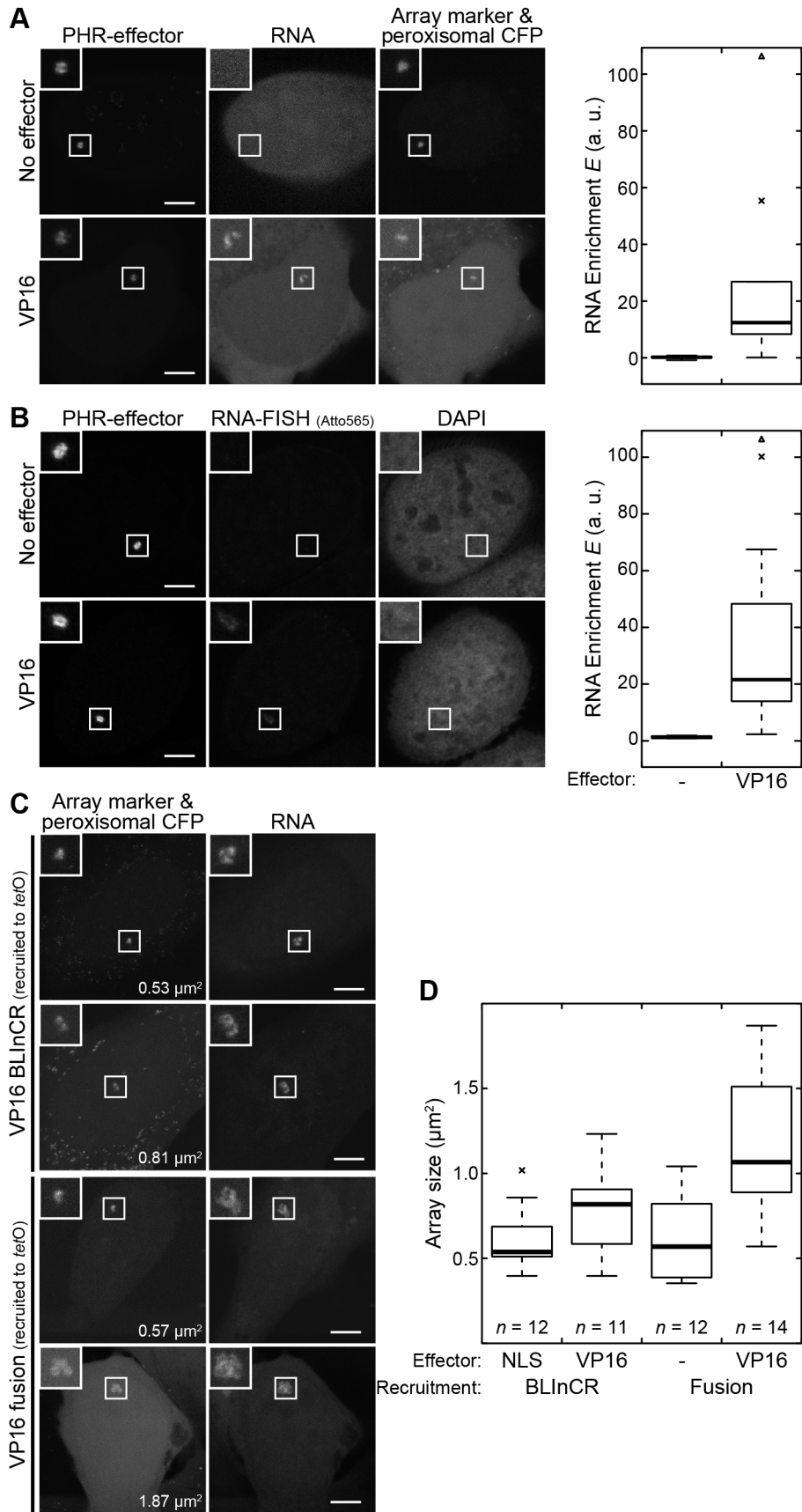
Supplementary information available online at <http://jcs.biologists.org/lookup/doi/10.1242/jcs.205534.supplemental>

**References**

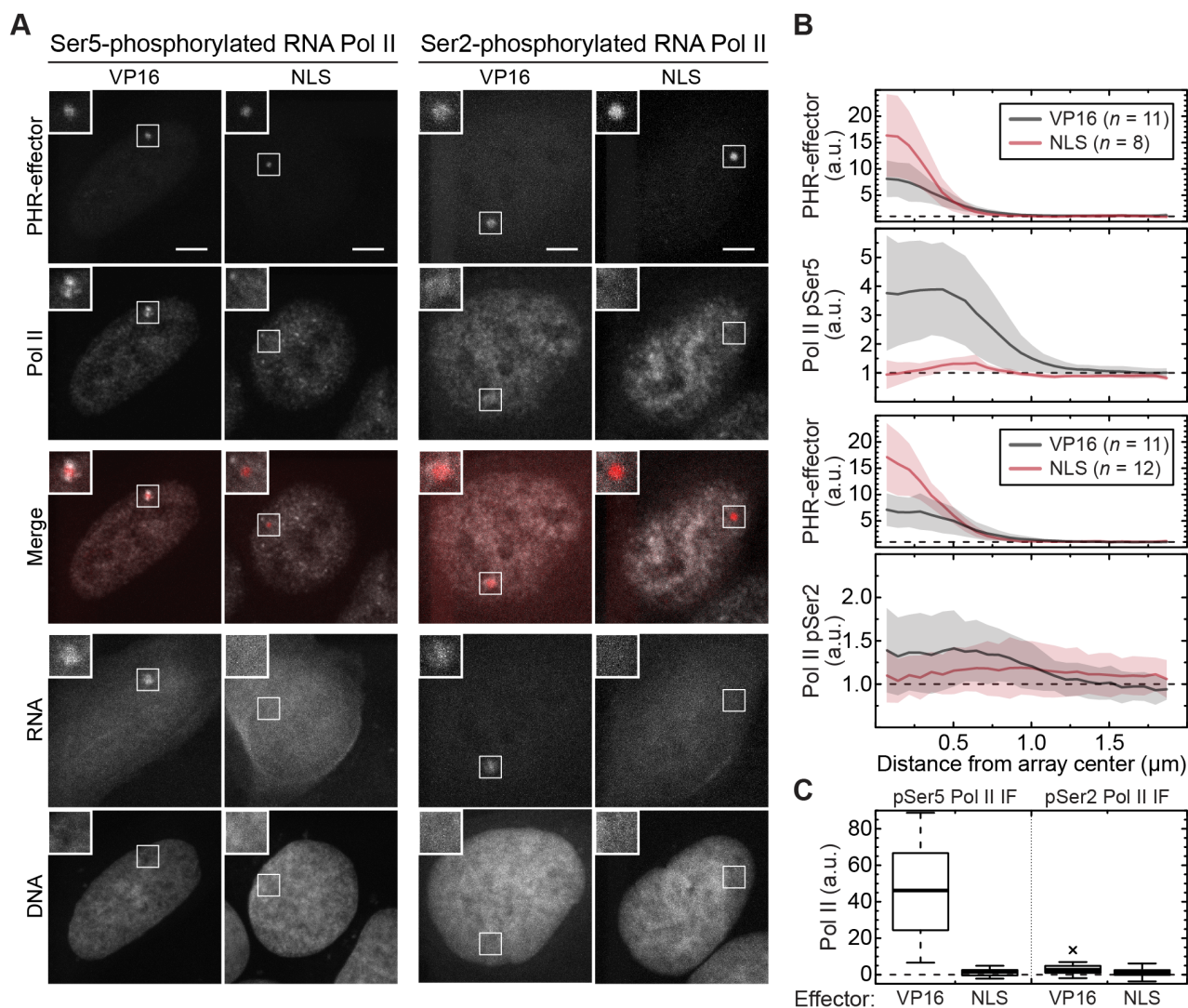
- Auslander, S., Auslander, D., Muller, M., Wieland, M. and Fussenegger, M. (2012). Programmable single-cell mammalian biocomputers. *Nature* **487**, 123–127.
- Bintu, L., Yong, J., Antebi, Y. E., McCue, K., Kazuki, Y., Uno, N., Oshimura, M. and Elowitz, M. B. (2016). Dynamics of epigenetic regulation at the single-cell level. *Science* **351**, 720–724.
- Boeger, H., Griesenbeck, J. and Kornberg, R. D. (2008). Nucleosome retention and the stochastic nature of promoter chromatin remodeling for transcription. *Cell* **133**, 716–726.
- Bugaj, L. J., Choksi, A. T., Mesuda, C. K., Kane, R. S. and Schaffer, D. V. (2013). Optogenetic protein clustering and signaling activation in mammalian cells. *Nat. Methods* **10**, 249–252.
- Carpenter, A. E., Memedula, S., Plutz, M. J. and Belmont, A. S. (2005). Common effects of acidic activators on large-scale chromatin structure and transcription. *Mol. Cell. Biol.* **25**, 958–968.
- Caudron-Herger, M., Pankert, T., Seiler, J., Nemeth, A., Voit, R., Grummt, I. and Rippe, K. (2015). Alu element-containing RNAs maintain nucleolar structure and function. *EMBO J.* **34**, 2758–2774.
- Cho, W. K., Jayanth, N., English, B. P., Inoue, T., Andrews, J. O., Conway, W., Grimm, J. B., Spille, J. H., Lavis, L. D., Lionnet, T. et al. (2016). RNA Polymerase II cluster dynamics predict mRNA output in living cells. *Elife* **5**, e13617.
- Choudhary, C., Kumar, C., Gnad, F., Nielsen, M. L., Rehman, M., Walther, T. C., Olsen, J. V. and Mann, M. (2009). Lysine acetylation targets protein complexes and co-regulates major cellular functions. *Science* **325**, 834–840.
- Chung, I., Leonhardt, H. and Rippe, K. (2011). De novo assembly of a PML nuclear subcompartment occurs through multiple pathways and induces telomere elongation. *J. Cell Sci.* **124**, 3603–3618.
- Cremer, T., Cremer, M., Hübner, B., Strickfaden, H., Smeets, D., Popken, J., Sterr, M., Markaki, Y., Rippe, K. and Cremer, C. (2015). The 4D nucleome: Evidence for a dynamic nuclear landscape based on co-aligned active and inactive nuclear compartments. *FEBS Lett.* **589**, 2931–2943.
- Darzacq, X., Shav-Tal, Y., de Turris, V., Brody, Y., Shenoy, S. M., Phair, R. D. and Singer, R. H. (2007). In vivo dynamics of RNA polymerase II transcription. *Nat. Struct. Mol. Biol.* **14**, 796–806.
- Darzacq, X., Yao, J., Larson, D. R., Causse, S. Z., Bosanac, L., de Turris, V., Ruda, V. M., Lionnet, T., Zenklusen, D., Guglielmi, B. et al. (2009). Imaging transcription in living cells. *Annu. Rev. Biophys.* **38**, 173–196.
- Dobin, A., Davis, C. A., Schlesinger, F., Drenkow, J., Zaleski, C., Jha, S., Batut, P., Chaisson, M. and Gingeras, T. R. (2013). STAR: ultrafast universal RNA-seq aligner. *Bioinformatics* **29**, 15–21.
- Filonov, G. S., Piatkevich, K. D., Ting, L.-M., Zhang, J., Kim, K. and Verkhusha, V. V. (2011). Bright and stable near-infrared fluorescent protein for in vivo imaging. *Nat. Biotechnol.* **29**, 757–761.
- Goodier, J. L., Mandal, P. K., Zhang, L. and Kazazian, H. H. Jr. (2010). Discrete subcellular partitioning of human retrotransposon RNAs despite a common mechanism of genome insertion. *Hum. Mol. Genet.* **19**, 1712–1725.
- Günther, K., Rust, M., Leers, J., Boettger, T., Scharfe, M., Jarek, M., Bartkuhn, M. and Renkawitz, R. (2013). Differential roles for MBD2 and MBD3 at methylated CpG islands, active promoters and binding to exon sequences. *Nucleic Acids Res.* **41**, 3010–3021.
- Janicki, S. M., Tsukamoto, T., Salghetti, S. E., Tansey, W. P., Sachidanandam, R., Prasanth, K. V., Ried, T., Shav-Tal, Y., Bertrand, E., Singer, R. H. et al. (2004). From silencing to gene expression: real-time analysis in single cells. *Cell* **116**, 683–698.
- Jegou, T., Chung, I., Heuvelman, G., Wachsmuth, M., Gorisch, S. M., Greulich-Bode, K. M., Boukamp, P., Lichter, P. and Rippe, K. (2009). Dynamics of telomeres and promyelocytic leukemia nuclear bodies in a telomerase-negative human cell line. *Mol. Biol. Cell* **20**, 2070–2082.
- Johnstone, R. W. and Licht, J. D. (2003). Histone deacetylase inhibitors in cancer therapy: is transcription the primary target? *Cancer Cell* **4**, 13–18.
- Kalderon, D., Roberts, B. L., Richardson, W. D. and Smith, A. E. (1984). A short amino-acid sequence able to specify nuclear location. *Cell* **39**, 499–509.
- Kennedy, M. J., Hughes, R. M., Peteya, L. A., Schwartz, J. W., Ehlers, M. D. and Tucker, C. L. (2010). Rapid blue-light-mediated induction of protein interactions in living cells. *Nat. Methods* **7**, 973–975.
- Konermann, S., Brigham, M. D., Trevino, A. E., Hsu, P. D., Heidenreich, M., Cong, L., Platt, R. J., Scott, D. A., Church, G. M. and Zhang, F. (2013). Optical control of mammalian endogenous transcription and epigenetic states. *Nature* **500**, 472–476.
- Langmead, B., Trapnell, C., Pop, M. and Salzberg, S. L. (2009). Ultrafast and memory-efficient alignment of short DNA sequences to the human genome. *Genome Biol.* **10**, R25.
- Larson, D. R., Fritzsche, C., Sun, L., Meng, X., Lawrence, D. S. and Singer, R. H. (2013). Direct observation of frequency modulated transcription in single cells using light activation. *Elife* **2**, e00750.
- Lau, I. F., Filipe, S. R., Søballe, B., Økstad, O.-A., Barre, F.-X. and Sherratt, D. J. (2003). Spatial and temporal organization of replicating Escherichia coli chromosomes. *Mol. Microbiol.* **49**, 731–743.
- Lerin, C., Rodgers, J. T., Kalume, D. E., Kim, S.-H., Pandey, A. and Puigserver, P. (2006). GCN5 acetyltransferase complex controls glucose metabolism through transcriptional repression of PGC-1 $\alpha$ . *Cell Metab.* **3**, 429–438.
- Li, G., Ruan, X., Auerbach, R. K., Sandhu, K. S., Zheng, M., Wang, P., Poh, H. M., Goh, Y., Lim, J., Zhang, J. et al. (2012). Extensive promoter-centered chromatin interactions provide a topological basis for transcription regulation. *Cell* **148**, 84–98.
- Li, W., Notani, D. and Rosenfeld, M. G. (2016). Enhancers as non-coding RNA transcription units: recent insights and future perspectives. *Nat. Rev. Genet.* **17**, 207–223.
- Love, M. I., Huber, W. and Anders, S. (2014). Moderated estimation of fold change and dispersion for RNA-seq data with DESeq2. *Genome Biol.* **15**, 550.
- Martin, R. M., Rino, J., Carvalho, C., Kirchhausen, T. and Carmo-Fonseca, M. (2013). Live-cell visualization of pre-mRNA splicing with single-molecule sensitivity. *Cell reports* **4**, 1144–1155.
- Motta-Mena, L. B., Reade, A., Mallory, M. J., Glantz, S., Weiner, O. D., Lynch, K. W. and Gardner, K. H. (2014). An optogenetic gene expression system with rapid activation and deactivation kinetics. *Nat. Chem. Biol.* **10**, 196–202.
- Muller-Ott, K., Erdel, F., Matveeva, A., Mallm, J.-P., Rademacher, A., Hahn, M., Bauer, C., Zhang, Q., Kaltofen, S., Schotta, G. et al. (2014). Specificity, propagation, and memory of pericentric heterochromatin. *Mol. Syst. Biol.* **10**, 746.
- Ng, H. H., Robert, F., Young, R. A. and Struhl, K. (2003). Targeted recruitment of Set1 histone methylase by elongating Pol II provides a localized mark and memory of recent transcriptional activity. *Mol. Cell* **11**, 709–719.
- Niopek, D., Benzinger, D., Roensch, J., Draebing, T., Wehler, P., Eils, R. and Di Ventura, B. (2014). Engineering light-inducible nuclear localization signals for precise spatiotemporal control of protein dynamics in living cells. *Nat. Commun.* **5**, 4404.
- Nocetti, N. and Whitehouse, I. (2016). Nucleosome repositioning underlies dynamic gene expression. *Genes Dev.* **30**, 660–672.
- Normanno, D., Boudarène, L., Dugast-Darzacq, C., Chen, J., Richter, C., Proux, F., Bénichou, O., Voituriez, R., Darzacq, X. and Dahan, M. (2015). Probing the target search of DNA-binding proteins in mammalian cells using TetR as model searcher. *Nat. Commun.* **6**, 7357.
- Osterwald, S., Deeg, K. I., Chung, I., Parisotto, D., Wörz, S., Rohr, K., Erfle, H. and Rippe, K. (2015). PML induces compaction, TRF2 depletion and DNA damage signaling at telomeres and promotes their alternative lengthening. *J. Cell Sci.* **128**, 1887–1900.
- Otsu, N. (1979). A threshold selection method from gray-level histograms. *IEEE Trans. Syst. Man. Cyber.* **9**, 62–66.
- Pankert, T., Jegou, T., Caudron-Herger, M. and Rippe, K. (2017). Tethering RNA to chromatin for fluorescence microscopy based analysis of nuclear organization. *Methods* **123**, 89–101.
- Papantonis, A. and Cook, P. R. (2013). Transcription factories: genome organization and gene regulation. *Chem. Rev.* **113**, 8683–8705.
- Polstein, L. R. and Gersbach, C. A. (2015). A light-inducible CRISPR-Cas9 system for control of endogenous gene activation. *Nat. Chem. Biol.* **11**, 198–200.
- Rafalska-Metcalf, I. U., Powers, S. L., Joo, L. M., LeRoy, G. and Janicki, S. M. (2010). Single cell analysis of transcriptional activation dynamics. *PLoS ONE* **5**, e10272.
- Schindelin, J., Arganda-Carreras, I., Frise, E., Kaynig, V., Longair, M., Pietzsch, T., Preibisch, S., Rueden, C., Saalfeld, S., Schmid, B. et al. (2012). Fiji: an open-source platform for biological-image analysis. *Nat. Methods* **9**, 676–682.
- Schneider, C. A., Rasband, W. S. and Eliceiri, K. W. (2012). NIH Image to ImageJ: 25 years of image analysis. *Nat. Methods* **9**, 671–675.
- Shahrezaei, V. and Swain, P. S. (2008). Analytical distributions for stochastic gene expression. *Proc. Natl. Acad. Sci. USA* **105**, 17256–17261.
- Shechter, D., Dormann, H. L., Allis, C. D. and Hake, S. B. (2007). Extraction, purification and analysis of histones. *Nat. Protoc.* **2**, 1445–1457.
- Sing, C. E., Olvera de la Cruz, M. and Marko, J. F. (2014). Multiple-binding-site mechanism explains concentration-dependent unbinding rates of DNA-binding proteins. *Nucleic Acids Res.* **42**, 3783–3791.
- Steinfeld, J. I., Francisco, J. S. and Hase, W. L. (1989). *Chemical Kinetics and Dynamics*. Englewood Cliffs, NJ: Prentice Hall.
- Sugaya, K., Vigneron, M. and Cook, P. R. (2000). Mammalian cell lines expressing functional RNA polymerase II tagged with the green fluorescent protein. *J. Cell Sci.* **113**, 2679–2683.
- Therizols, P., Illingworth, R. S., Courilleau, C., Boyle, S., Wood, A. J. and Bickmore, W. A. (2014). Chromatin decondensation is sufficient to alter nuclear organization in embryonic stem cells. *Science* **346**, 1238–1242.

- Thevenaz, P., Ruttimann, U. E. and Unser, M.** (1998). A pyramid approach to subpixel registration based on intensity. *IEEE Trans. Image Process.* **7**, 27-41.
- Tischer, D. and Weiner, O. D.** (2014). Illuminating cell signalling with optogenetic tools. *Nat. Rev. Mol. Cell Biol.* **15**, 551-558.
- Tumbar, T., Sudlow, G. and Belmont, A. S.** (1999). Large-scale chromatin unfolding and remodeling induced by VP16 acidic activation domain. *J. Cell Biol.* **145**, 1341-1354.
- Untergasser, A., Cutcutache, I., Koressaar, T., Ye, J., Faircloth, B. C., Remm, M. and Rozen, S. G.** (2012). Primer3—new capabilities and interfaces. *Nucleic Acids Res.* **40**, e115.
- Villar-Garea, A., Israel, L. and Imhof, A.** (2008). Analysis of histone modifications by mass spectrometry. *Curr Protoc Protein Sci.* Chapter 14, Unit 14 10.
- Zhang, T., Cooper, S. and Brockdorff, N.** (2015). The interplay of histone modifications - writers that read. *EMBO Rep.* **16**, 1467-1481.

## Supplementary Figures

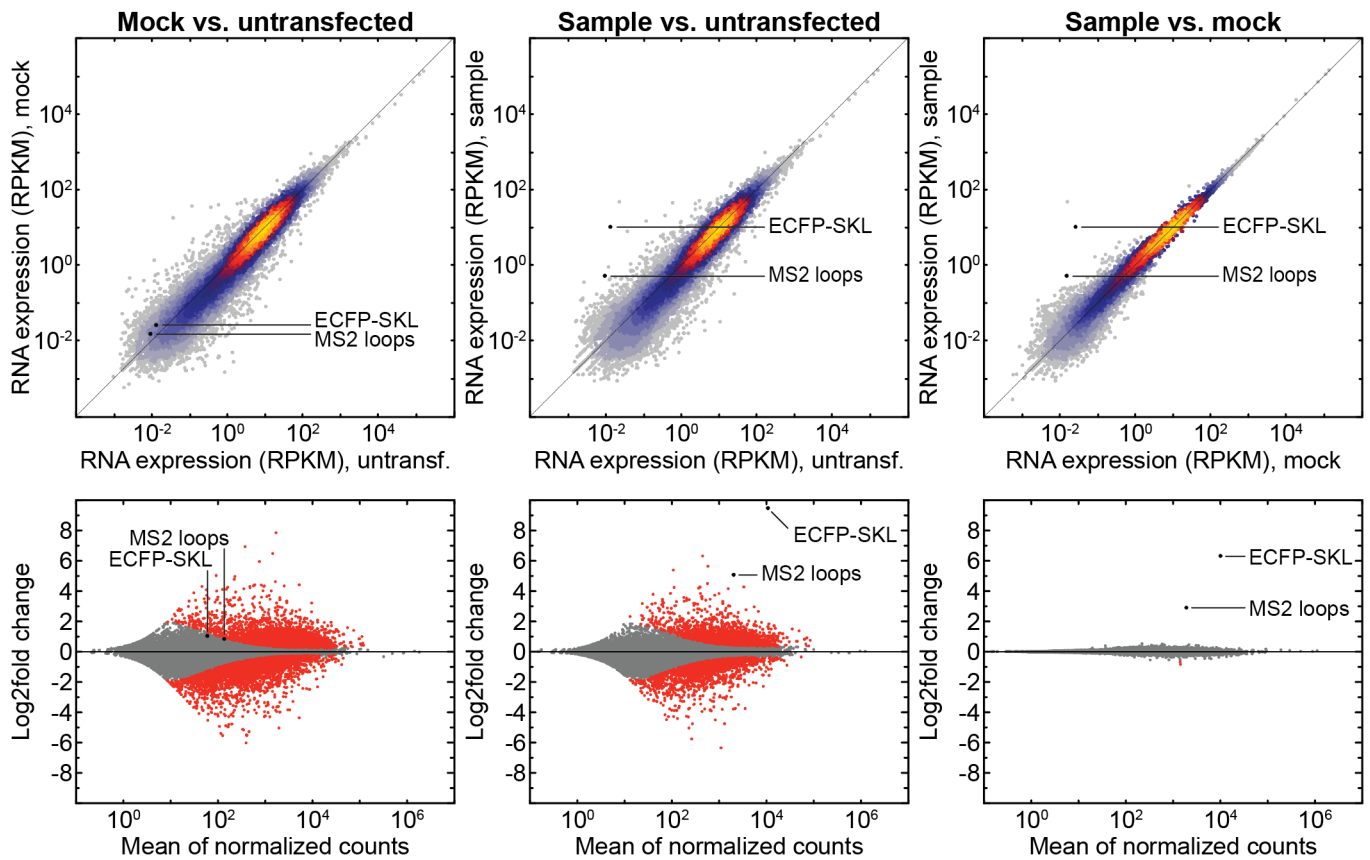


**Supplementary Figure S1. Continuous light-dependent recruitment of PHR-YFP-VP16 to reporter array.** Cells were continuously illuminated overnight with a blue LED, leading to recruitment of PHR constructs (via CIBN-TetR) to the *tetO* repeats of the reporter array. In the control reaction (“no effector”) transfection was with PHR-YFP instead of PHR-YFP-VP16. **(A)** Maximum intensity projection CLSM images of YFP-labeled effectors, RNA (visualized via mKate2-MCP), an array marker (CFP-LacI) and peroxisomal CFP. Quantification of RNA enrichment is shown on the right ( $n=9$  for each condition). **(B)** Same as in panel A, but RNA stained by RNA-FISH ( $n = 6$  and  $n = 11$  for the control without effector and VP16, respectively). The amount of RNA detected at the array after VP16 recruitment showed a similar distribution for different RNA detection methods (compare quantification for panels A and B) and varied considerably across different cells. **(C)** Exemplary maximum intensity projection CLSM images visualizing the array through the independent marker CFP-LacI. VP16 was either recruited via BLInCR (by transfecting PHR-YFP-VP16 & CIBN-TetR) or with a fusion construct (GFP-TetR-VP16). All cells transfected with a VP16 construct showed mKate2-MCP enrichment, confirming that these cells were transcriptionally active. **(D)** Quantification of array sizes with enriched VP16 (shown in panel C) compared to negative controls without VP16 (i.e., PHR-YFP-NLS for BLInCR and TetR-GFP as a fusion construct). On average, cells expressing TetR-VP16 fusion constructs had somewhat larger arrays compared to cells with constitutive optogenetic recruitment of VP16. Notably, some of the activated cells in the latter population had condensed arrays that were comparable to those in the negative control PHR-YFP-NLS. Scale bars: 5  $\mu\text{m}$ .

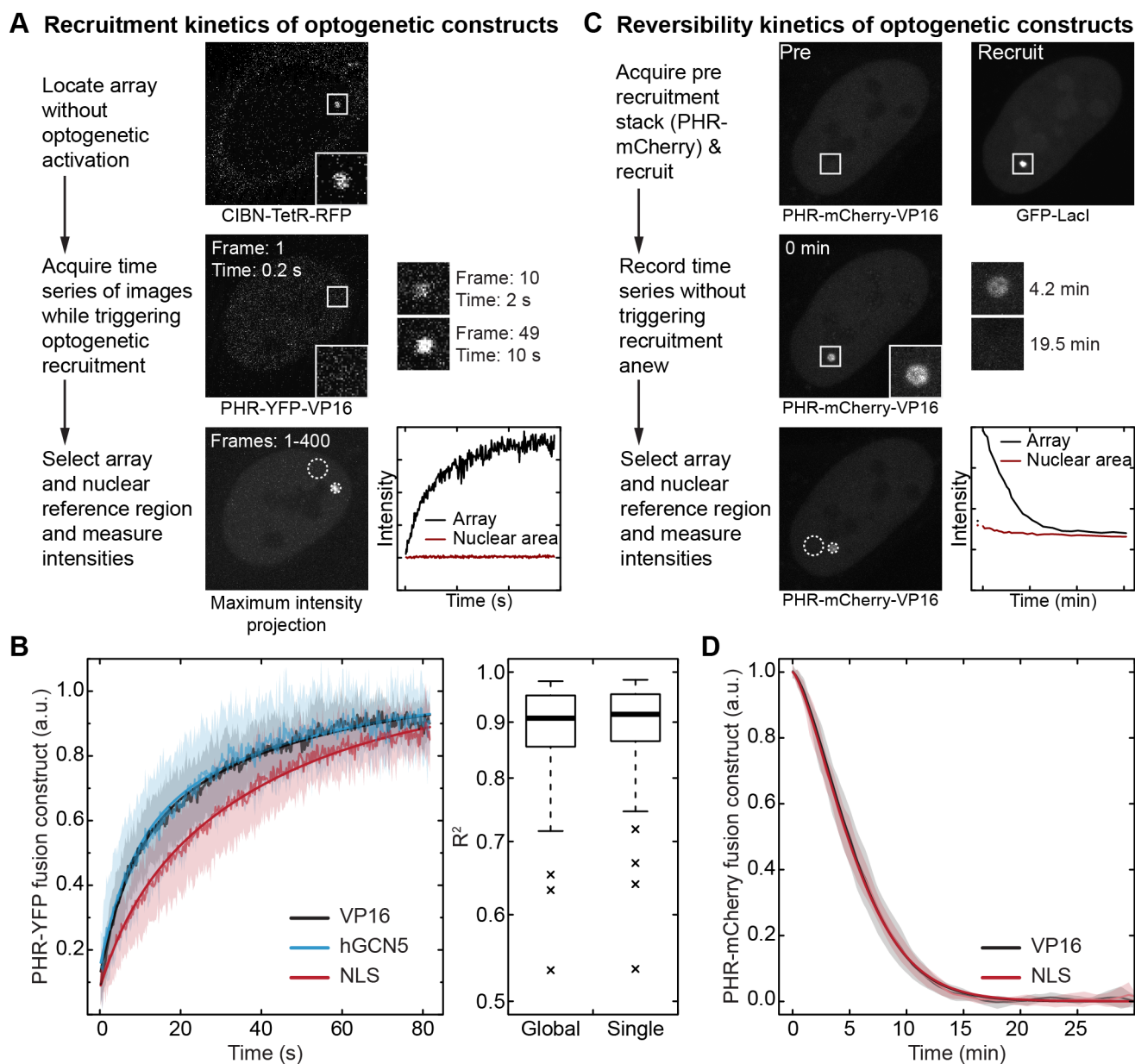


**Supplementary Figure S2. Immunostaining of RNA polymerase II phosphorylated at serine 2 or 5.** Cells were transfected with PHR-YFP-effector constructs, CIBN-TetR and mKate2-MCP to monitor RNA production. The respective pol II species were visualized with the primary antibodies and the Alexa647-labeled secondary antibody listed in the Methods section. DNA was counterstained with DAPI. **(A)** Exemplary maximum intensity projections of CLSM images showing that neither the initiating serine 5-phosphorylated (Ser5p) pol II nor the elongating serine 2-phosphorylated (Ser2p) pol II could be detected in non-activated control cells. Ser5p was clearly enriched in activated cells, whereas Ser2p was only slightly accumulated at the array. The absence of pol II Ser2p signal in most cells might be due to the small size of the transgene of ~3 kb. Reportedly, Ser2p tends to occur downstream of Ser5p and is only observed beyond 3 kb for some genes (Descostes et al. 2014, eLife 3, e02105). Scale bars: 5  $\mu\text{m}$ . **(B)** Average DAPI-normalized radial intensity profiles around the array. Quantifications of transfected cells was done as described in panel A. **(C)** Total accumulated pol II signal calculated from the radial profiles ( $\sum_{r=0}^{r=\text{FWHM}} 2\pi r I(r)$ ),

where  $r$  is the distance from the array center, FWHM the full width at half maximum calculated from the effector profiles and  $I(r)$  the intensity at distance  $r$  from the radial profiles in panel B).

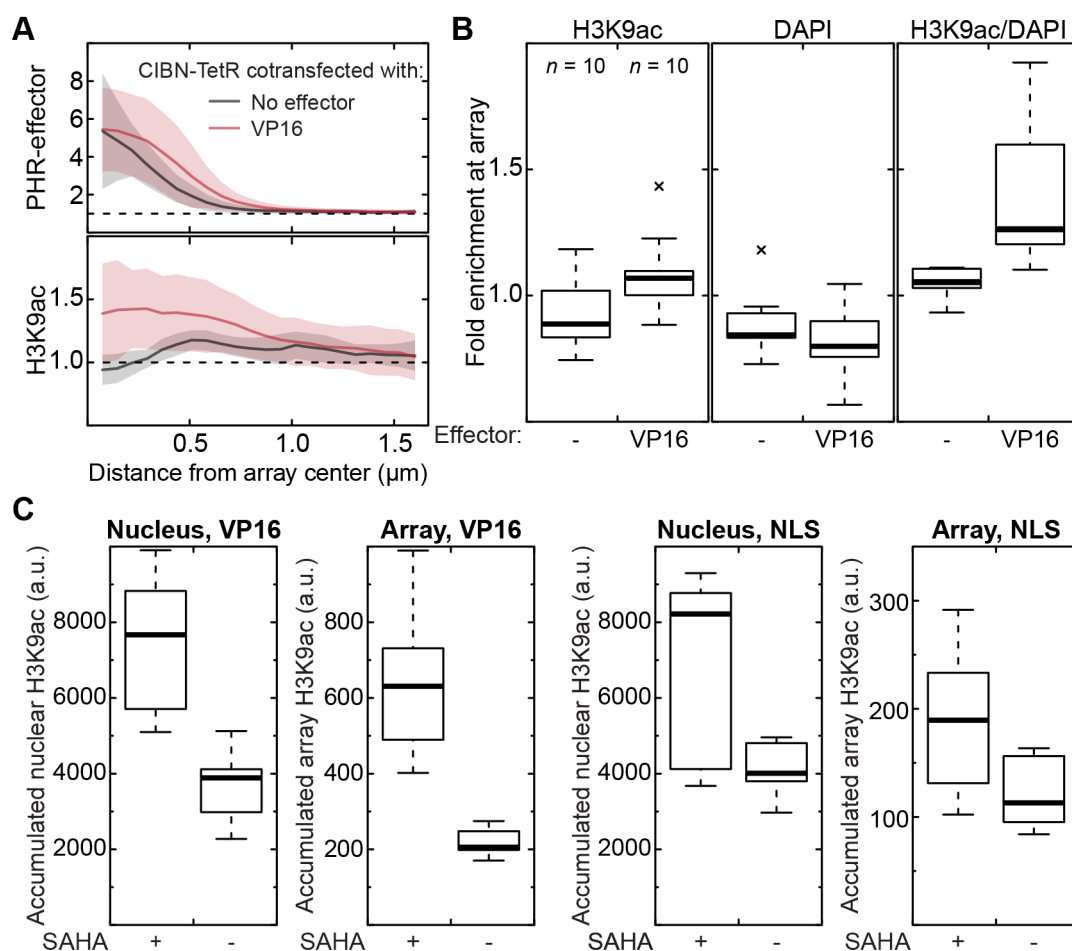


**Supplementary Figure S3. Gene expression in U2OS 2-6-3 cells transfected with different constructs.** Cells were transfected with YFP and TetR-RFP (mock) or PHR-YFP-VP16, CIBN-TetR and mCherry-MCP (sample). The upper set of plots shows RPKM values for annotated genes in mock vs. untransfected (left), sample vs. untransfected (center) and sample vs. mock (right) cells. The lower set of plots are MA plots derived from the differential gene expression analysis with DESeq2 for the respective combination. When comparing mock or sample vs. untransfected cells, hundreds of genes were differentially expressed, indicating that either expression of TetR or the transfection procedure itself causes substantial changes in gene expression. However, when comparing sample to mock-transfected cells, only the reporter elements (MS2 loops and ECFP-SKL) showed significant differential expression ( $p_{\text{adj}} < 0.001$ ) and log<sub>2</sub>-fold changes  $> 1$ .



**Supplementary Figure S4. Recruitment and reversibility with BLInCR.** (A) The typical workflow of a BLInCR experiment is illustrated for cells transfected with CIBN-TetR-tagRFP-T (localizer) and PHR-YFP-VP16 (effector). First, the cellular structure bound by the localizer (here: *tetO* array) was located in the tagRFP-T channel (excitation with yellow-green light), which did not trigger optogenetic recruitment. Next, a YFP time series was recorded while triggering recruitment of the effector to the localizer (excitation with blue light). Finally, the structure that was targeted by the localizer (here: *tetO* array) and a nuclear reference region were selected in the maximum intensity projection of the time series and the mean intensities at those regions were measured for each image. (B) Recruitment kinetics of PHR-YFP-fused effector proteins (left). Experimental means (solid lines, light), standard deviations (shaded areas) and fits (solid lines, dark) are shown. A global fit using the same two rate constants for all curves (and all constructs) yielded similar fit qualities as fits of each single curve with individual rate constants (right). In particular, the cumulative residual

sum of squares was only 8.5% larger for the global fit. The fit parameters for the global fit and the number of cells for each construct are listed in **Supplementary Table S2**. **(C)** A typical workflow for a BLInCR reversibility experiment is illustrated for cells transfected with CIBN-TetR (localizer), GFP-LacI (marker) and PHR-mCherry-VP16 (effector). A stack of images was recorded in the mCherry channel (excitation with yellow-orange light) prior to recruitment. The array was visualized by recording two stacks in the marker channel with blue light excitation for 38 s, thereby triggering effector recruitment to the localizer. The dissociation of the effector from the targeted structure was monitored by recording image stacks every 30-120 s without triggering the PHR switch again (excitation with yellow-orange light). Finally, the targeted structure and a nuclear reference region were selected in the maximum intensity projection of the time series and the mean intensities at those regions were measured for each image. **(D)** Plot of experimental means (solid lines, light), standard deviations (shaded areas) and fits of average curves (solid lines, dark). Averages of fit parameters obtained from fitting the single curves and the number of cells for each construct are listed in **Supplementary Table S3**.



### Supplementary Figure S5. Local histone acetylation levels.

(A) Average radial intensity profiles from maximum projections of CLSM images. Cells were transfected with CIBN-TetR and a YFP-labeled PHR-effector construct. The effector constructs (top) and the H3K9ac staining (IF with Alexa568-labeled secondary antibody) are shown. When VP16 was absent, there was a drop in H3K9ac levels compared to the surrounding chromatin, which was not present when VP16 was recruited (bottom). Conversely, there was a slight drop in DNA density when VP16 was present, possibly indicating array decondensation (see **Supplementary Fig. S1C** and panel B). (B) Fold enrichment of H3K9ac and DNA density (DAPI) at the array compared to a nuclear reference region. The DAPI-normalized H3K9ac fold enrichment is depicted on the right. It increased when VP16 was present, indicating that the array became acetylated when activated. The fold enrichments were taken from the center of the radial profiles (shown in panel A for H3K9ac). (C) Absolute fluorescence intensity of H3K9ac IF staining in the entire nucleus and at the array under different conditions. Cells were grown in a removable 4-well culture insert, which allows for culturing cells under different conditions on the same slide. Cells were transfected with CIBN-TetR for recruitment, mKate2-MCP to assess transcriptional activity, and either PHR-YFP-NLS or PHR-YFP-VP16. In addition, cells were either treated with 2  $\mu\text{M}$  SAHA or left untreated as a control

(VP16,  $n = 12/12$ , NLS,  $n = 6/8$  for treated/untreated cells, respectively). H3K9ac was stained using IF with the primary and secondary Alexa633-labeled antibodies listed in the Methods section. IF stainings were done on the same slide (after removing the culture insert) and images were recorded on the same day with identical imaging settings so that absolute intensities can be directly compared. As expected, SAHA led to increased nuclear and array H3K9ac levels both in activated and non-activated cells. Intensity levels at the array were calculated as in **Supplementary Fig. 2C** and are normalized to DAPI density.

## Supplementary Tables

**Supplementary Table S1. List of BLInCR constructs.**

CIBN constructs	PHR constructs	Others
<b>CIBN-tagBFP-TetR</b>	<b>PHR-mCherry</b>	tagBFP-LacI
CIBN-YFP-TetR	<b>PHR-iRFP713</b>	<b>CFP-LacI</b>
<b>CIBN-tagBFP-hLaminB1</b>	PHR-YFP	<b>GFP-LacI</b>
CIBN-YFP-hLaminB1	<b>PHR-mCherry-NLS</b>	RFP-LacI
CIBN-tagBFP-hTRF1	<b>PHR-YFP-NLS</b>	<b>TetR-GFP</b>
CIBN-YFP-hTRF1	<b>PHR-mCherry-VP16</b>	TetR-YFP
<b>CIBN-tagBFP-hTRF2</b>	<b>PHR-YFP-VP16</b>	TetR-mRFP
CIBN-YFP-hTRF2	<b>PHR-iRFP713-VP16</b>	GFP-MCP
<b>CIBN-tagBFP-hNCL</b>	PHR-mCherry-hPMLIII	<b>tagRFP-MCP</b>
CIBN-YFP-hNCL	PHR-YFP-hPMLIII	<b>mKate2-MCP</b>
<b>CIBN-tagBFP-hPMLIII</b>	<b>PHR-YFP-hGCN5</b>	mCherry-MCP
CIBN-YFP-hPMLIII	PHR-YFP-hGCN5-NLS	tagBFP-TetR-VP16
<b>CIBN-TetR-tagRFP-T</b>	PHR-YFP-hGCN5mut	GFP-TetR-VP16
CIBN-LacI-tagRFP-T	PHR-YFP-hHP1 $\beta$	tagBFP-LacI-VP16
CIBN-hTRF1-tagRFP-T	PHR-mCherry-hHP1 $\beta$	GFP-LacI-VP16
CIBN-hTRF2-tagRFP-T		
<b>CIBN-TetR</b>		
CIBN-LacI		
CIBN-YFP		
CIBN-mCherry		

For developing BLInCR, constructs with different autofluorescent protein domain fusions were constructed and tested. The constructs used for the experiments described in the main and supplementary figures are indicated in bold. All constructs have been deposited at the Addgene plasmid repository.

**Supplementary Table S2. Summary of kinetic parameters for optogenetic recruitment.**

	PHR-YFP-VP16	PHR-YFP-hGCN5	PHR-YFP-NLS
Number of cells $n$	18	18	19
$k_1$ (s <sup>-1</sup> ), fast reaction <sup>a</sup>		0.129 ± 0.003	
$b$ , fraction fast <sup>b</sup>	0.40 ± 0.16	0.39 ± 0.23	0.19 ± 0.20
$k_2$ (s <sup>-1</sup> ), slow reaction <sup>a</sup>		0.023 ± 0.001	
$c$ , fraction slow <sup>b</sup>	0.48 ± 0.17	0.47 ± 0.25	0.73 ± 0.21
$\tau_{1/2}$ (s) <sup>b</sup>	13.6 ± 4.9	14.2 ± 7.1	22.2 ± 7.7

Recruitment curves were fitted with a model describing two parallel first-order reactions ( $E(t) = a - b \cdot \exp(-k_1 \cdot t) - c \cdot \exp(-k_2 \cdot t)$ ). The recruitment rates  $k_1$  and  $k_2$  were fitted globally while the plateau value  $a$  and the fractions  $b$  and  $c$  were fitted individually for each cell to account for varying transfection efficiencies and differences between the recruited constructs. The plateau value  $a$  was used to normalize the curves.

<sup>a</sup> The fit parameters of the globally fitted rates and their standard fit errors are listed.

<sup>b</sup> The characteristic recruitment time  $\tau_{1/2}$  for reaching half maximal levels and the contributions of the fast and slow reactions were computed as averages and standard deviations of all single values.

**Supplementary Table S3. Summary of kinetic parameters for dissociation after optogenetic recruitment.**

	PHR-mCherry-VP16	PHR-mCherry-NLS
Number of cells $n$	13	12
$k$ (min <sup>-1</sup> )	0.07 ± 0.04	0.08 ± 0.03
$m$	1.53 ± 0.20	1.47 ± 0.22
$t_{1/2}$ (min)	4.9 ± 0.8	4.8 ± 0.6

Single reversibility curves were fitted with an exponential model comprising a time-dependent reaction rate ( $E(t) = a \cdot \exp(-k \cdot t^m) + c$ ). Mean and standard deviation are shown.

**Supplementary Table S4. Fit parameters for different models of BLInCR-induced transcription activation.**

Two-state model			Feedback model			Sequential model		
	untreated	SAHA		untreated	SAHA		untreated	SAHA
$A_0$ (%)	0	7	$A_{1,0}$ (%)	0.6	0.1	$A_0$ (%)	9	27
$k_a$ ( $\text{min}^{-1}$ )	0.0042	0.0008	$A_2$ (%)	8	33	$n$	7	11
$k_i$ ( $\text{min}^{-1}$ )	0.011	0.002	$k_a$ ( $\text{min}^{-1}$ )	0.15	0.26	$k_a$ ( $\text{min}^{-1}$ )	0.16	0.23
$k_r$ ( $\text{min}^{-1}$ )	0.32	0.33	$k_r$ ( $\text{min}^{-1}$ )	0.61	0.54	$k_r$ ( $\text{min}^{-1}$ )	0.89	0.82
$k_d$ ( $\text{min}^{-1}$ )		0.017	$k_d$ ( $\text{min}^{-1}$ )		0.50	$k_d$ ( $\text{min}^{-1}$ )		0.62
Fit quality		0.9714	Fit quality		0.9992	Fit quality		0.9985

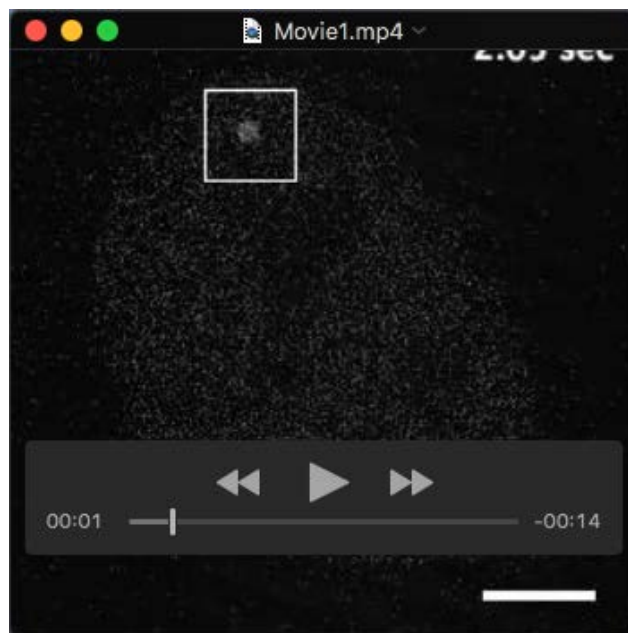
Differential equations and their solution are described in the Methods section. Averaged curves and fit curves are depicted in **Fig. 4A**. The fit quality corresponds to the adjusted coefficient of determination  $R^2$ .

**Supplementary Table S5. Antibodies used in this study.**

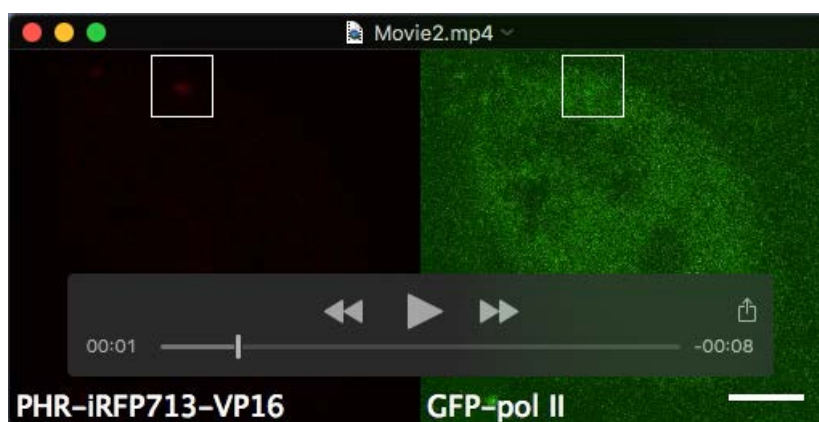
Target	Host	Dilution	Source
<i>Primary antibodies</i>			
H3K9ac	Rabbit	1:1000 (IF)	ActiveMotif #39917, lot 16111002 ( <b>Fig. S5A,B</b> ) and lot 23913004 ( <b>Fig. S5C</b> )
		1:1000 (WB)	ActiveMotif #39137, lot: 09811002
H3K27ac	Rabbit	1:1000 (WB)	Abcam #4729, lot: CR238071-2
H4ac	Rabbit	1:2000 (WB)	Millipore #06-866, lot: DAM1416550
H3	Mouse	1:1000 (WB)	Cell Signaling Technology #14269, lot: 20
GFP	Rabbit	1:500 (IF)	Abcam #290, lot: GR135929-1
RNA pol II CTD phospho Ser2	Rat	1:100 (IF)	Clone 3E10, ActiveMotif #61083, lot: 20212002
RNA pol II CTD phospho Ser5	Rat	1:100 (IF)	Clone 3E8, ActiveMotif #61085, lot: 16513002
<i>Secondary antibodies</i>			
Rabbit IgG, HRP-linked	Goat	1:2000 (WB)	Cell Signaling Technology #7074, lot: 25
Mouse IgG, HRP-linked	Horse	1:2000 (WB)	Cell Signaling Technology #7076, lot: 27
Rabbit IgG, Alexa 488-linked	Goat	1:500 (IF)	Life Technologies #A11034, lot: 1141875
Rabbit IgG Alexa 568-linked	Goat	1:500 (IF)	Life Technologies #A11036, lot: 997761
Rabbit IgG Alexa 633-linked	Goat	1:500 (IF)	Life Technologies #A21071, lot: 51445A
Rat IgG Alexa 647-linked	Goat	1:500 (IF)	Life Technologies #A21247, lot: 1884217

IF: immunofluorescence, WB: western blot.

## Supplementary Movies



**Movie 1. Light-dependent recruitment of PHR-YFP-VP16 to tethered CIBN-TetR.** Note that the brightness has been adjusted non-linearly (gamma = 0.65) for better visibility of the signals at the array and within the nucleoplasm. Speed: 10 fps (~2x). Scale bar: 5  $\mu$ m. The movie is provided as a separate file in mp4 format.



**Movie 2. Co-recruitment of GFP-tagged RNA polymerase II.** Note that the brightness has been adjusted non-linearly (gamma = 0.65) for better visibility of the signals at the array and within the nucleoplasm. PHR-VP16 was tagged with far-red iRFP713. Speed: 4 fps (~20x). Scale bar: 5  $\mu$ m. The movie is provided as a separate file in mp4 format.